

1 **Moisture sources and dynamics over southeastern Tibetan Plateau** 2 **reflected in dual water vapor isotopes**

3
4 Zhongyin Cai^{1*}, Rong Li¹, Cheng Wang¹, Qiukai Mao¹, Lide Tian¹

5
6 ¹Institute of International Rivers and Eco-security, Yunnan Key Laboratory of International Rivers and
7 Transboundary Eco-security, Ministry of Education Key Laboratory for Ecoscurity of Southwest China, Yunnan
8 University, Kunming, China

9
10 *Corresponding author: Zhongyin Cai (czypil@gmail.com and z.cai@ynu.edu.cn)

11 12 **Abstract**

13 The southeastern Tibetan Plateau (SETP) has experienced a significant drying trend in recent decades, likely
14 linked to shifts in moisture sources. To investigate the role of ocean surface evaporation, continental air mass
15 intrusion, and rain-vapor interaction, we present a three-year daily time series of near-surface vapor $\delta^{18}\text{O}$ and d -
16 excess from the SETP station. Our analysis reveals that apparent negative correlations between d -excess and relative
17 humidity over the Indian Ocean are primarily driven by similar seasonal patterns, which become insignificant or
18 marginal when examined seasonally. This result underscores the need for caution in interpreting d -excess as a
19 conservative tracer of ocean surface evaporation. Instead, we identify local and upstream specific humidity as the
20 primary determinant of non-monsoon season d -excess variability, influenced by the intrusion of cold and dry air
21 from upper levels. During the summer monsoon season, both d -excess and $\delta^{18}\text{O}$ reflect the effect of raindrop

evaporation during transport, which decreases $\delta^{18}\text{O}$ but increases *d*-excess. These findings offer new insights into using water isotopes to track moisture sources and dynamics across SETP, especially under varying seasonal circulation systems. Particularly, the findings for *d*-excess will contribute to our understanding of different moisture sources and provide a framework for interpreting *d*-excess in various hydroclimatic applications, including ice core studies.

1 Introduction

The Tibetan Plateau (TP) and its surrounding regions, known as the Third Pole and the Asian Water Tower, is a critical source of freshwater for billions of people (Immerzeel et al., 2020; Yao et al., 2022). Recent climate change has induced significant hydrological shifts, marked by drying trends in the southeastern TP (SETP) and wetting in the north (Jiang et al., 2023; Zhang et al., 2023; Yao et al., 2022). Atmospheric water vapor is the primary input to the hydrological system, making it essential to understand its sources and dynamics to diagnose regional water imbalances. Using a Lagrangian vapor tracking method, Zhang et al. (2023) suggested that the drying trend is associated with meteorological droughts propagating from moisture source regions. However, their conclusions and methodology are subjects of ongoing debate (Zhang et al., 2025; Zhao et al., 2025), underscoring the need for alternative approaches. As natural tracer of the water cycle, water stable isotopes offer valuable insights into moisture sources and dynamics (Bowen et al., 2019; Galewsky et al., 2016). However, the interpretation of these isotopic signals on the TP remains challenging due to complex fractionation processes and shifting circulation systems between summer monsoon and westerlies (Yao et al., 2013; Thompson et al., 2024; Bershaw, 2018; Li et al., 2025).

Recent studies have confirmed that monsoon convection at upstream along moisture transport pathways, rather

than local precipitation amount, controls summer monsoon season precipitation $\delta^{18}\text{O}$ over southern TP (Cai et al., 2017; He et al., 2015). This is related to the “amount effect” (Dansgaard, 1964), where higher precipitation leads to lower $\delta^{18}\text{O}$ values due to continuous rainout associated with stronger convection, following the Rayleigh distillation (Kurita et al., 2015; Ruan et al., 2019; Cai et al., 2025). Additionally, interactions between rain and water vapor play a significant role in depleting the lower tropospheric vapor isotopes (Risi et al., 2008a; Kurita et al., 2011; Cai et al., 2018; Lee and Fung, 2008). While the regional amount effect prevails during the monsoon season, this relationship weakens or reverses in the non-monsoon season when it is dominated by westerlies. This variability suggests additional controls such as moisture source variability, kinetic fractionation, or shifts in atmospheric circulation patterns (Breitenbach et al., 2010; Cai and Tian, 2020; Guo et al., 2024; Yao et al., 2013).

Observations of vapor isotopes could help disentangle the different processes involved in the amount effect, particularly through examining the secondary parameter deuterium excess (*d*-excess). The *d*-excess, defined by Dansgaard (1964) as $\delta^2\text{H} - 8\delta^{18}\text{O}$, primarily reflects the effects of kinetic fractionation. During rainout process, equilibrium fractionation is the dominant mechanism, whereas raindrop evaporation is associated with kinetic fractionation. Further, limited precipitation during non-monsoon seasons makes it challenging to study a full seasonal cycle of the atmospheric water cycle, which can be compensated by continuous monitoring of vapor isotopes. While a few stations on the TP have monitored isotopic compositions in the vapor phase (Tian et al., 2020; Dai et al., 2021; Chen et al., 2024; Yu et al., 2016; Yu et al., 2015), there is limited knowledge about vapor *d*-excess.

Both theoretical predictions and observations over ocean surfaces indicate that *d*-excess reflects ocean surface evaporation conditions, such as sea surface temperature (SST) and relative humidity normalized to SST (RH_{SST}) (Merlivat and Jouzel, 1979; Bonne et al., 2019; Liu et al., 2014; Craig and Gordon, 1965). These relationships are frequently invoked to interpret *d*-excess over the TP (Zhao et al., 2012; Shao et al., 2021; Chen et al., 2024; Liu et al., 2024). For instance, Shao et al. (2021) found significant correlations between an ice core *d*-excess record from

65 the central TP and RH_{SST} over the northern Bay of Bengal (BOB) and Arabian Sea (AS). However, the correlation
66 coefficient was only -0.44 with a steep slope of $-0.99\text{‰}\text{‰}^{-1}$, which differs from the typical range observed in oceanic
67 regions ($-0.3\text{‰}\text{‰}^{-1}$ to $-0.6\text{‰}\text{‰}^{-1}$) (Bonne et al., 2019; Liu et al., 2014; Benetti et al., 2014; Uemura et al., 2008).
68 This discrepancy suggests additional complexities, such as continental recycling and raindrop evaporation.
69 Furthermore, many studies at other terrestrial sites have also questioned whether d -excess accurately preserves
70 evaporation conditions from oceanic source regions (Fiorella et al., 2018; Aemisegger et al., 2014; Welp et al., 2012;
71 Wei and Lee, 2019; Samuels - Crow et al., 2014).

72 In addition, ice core d -excess values at high altitudes are generally higher than those observed in precipitation
73 at lower altitudes on the TP (Shao et al., 2021; Tian et al., 2001; Zhao et al., 2012; Joswiak et al., 2013; Zhao et al.,
74 2017; Thompson et al., 2000). High vapor d -excess values at high elevations have been observed elsewhere, such
75 as on the Andes (Samuels - Crow et al., 2014). Such elevated d -excess values have been attributed to the mixing
76 with subsiding air (Samuels - Crow et al., 2014; Sodemann et al., 2017). However, this mechanism remains
77 unconfirmed on the TP.

78 Mountain valleys in the SETP have been considered as significant pathways for transporting water vapor into
79 the TP (Araguás-Araguás et al., 1998; Tian et al., 2007; Yao et al., 2013). To investigate these processes, we initiated
80 a water vapor sampling campaign at the South-East Tibetan Plateau Station for integrated observation and research
81 of alpine environment (SETP station) in June 2015. The primary objectives were to explore moisture sources and
82 dynamics and their influence on vapor isotope compositions across different seasons. To achieve these goals, we
83 analyzed the relationships between vapor isotopes and oceanic evaporation conditions, continental air mass
84 intrusions, as well as rain-vapor interactions during different seasons. Finally, we discuss how our findings
85 contribute to the interpretation of ice core records.

2 Data and methods

2.1 Atmospheric water vapor sampling

Vapor samples were collected at the SETP station (29°46'N, 94°44'E, 3326 m above sea level, and Fig. S1) using a cryogenic trapping method. The sampling system includes an air pump, a linked-ball-shaped glass cold trap, and an electric-powered system that creates and maintains a cold environment filled by 95% ethanol as cold as below -80 °C. Ambient air was pumped from an inlet positioned about 8 m above ground level through a Teflon tube to a glass trap maintained at an operational temperature of -70 °C. The airflow rate was set to ~5 L/min, allowing the collection of 10-20 ml of water samples during each sampling session. Sampling durations were adjusted seasonally: 24 hours in summer and extended to 48 hours in winter when necessary to ensure adequate sample volume. Samples were collected at 20:00 Beijing Standard Time (12:00 UTC). The efficiency of the trapping method was verified by connecting an additional cold trap to the system, which showed no visible condensation in the additional cold trap (Yu et al., 2015). Further validation was achieved through comparisons with direct measurements using a Picarro L2130-i Cavity Ring Down Spectroscopy (CRDS) at Lhasa, southern TP, confirming the reliability of this method for atmospheric water vapor sampling (Tian et al., 2020).

The sampling campaign ran from 25 June 2015 to 14 June 2018, yielding a total of 742 samples. These samples were stored frozen until analysis. Those collected before 28 June 2016 were measured at the Key Laboratory of Tibetan Plateau Earth System, Environment and Resources, Institute of Tibetan Plateau Research, Chinese Academy of Sciences by a Picarro L2130-i analyzer. Samples collected after 28 June 2016 were measured at the Institute of International River and Eco-security, Yunnan University by a Picarro L2140-i analyzer. The isotopic values were calibrated using three standard waters, with detailed calibration procedures described by Liu et al. (2024). The measurements are expressed relative to Vienna Standard Mean Ocean Water 2 (VSMOW2), with precisions of 0.1‰ for $\delta^{18}\text{O}$, 0.4‰ for $\delta^2\text{H}$, and 1.2‰ for d -excess.

108 **2.2 Meteorological data**

109 Daily local meteorological data prior to 2018, including precipitation amount, air temperature, air pressure,
110 and relative humidity at the SETP station, were obtained from the National Tibetan Plateau/Third Pole Environment
111 Data Center (Luo, 2018). Specific humidity (q) at the SETP station was calculated using air temperature, air pressure,
112 and relative humidity data following established equations outlined in (Huang, 2018).

113 We further obtained meteorological variables such as 2-meter air temperature, 2-meter dew point temperature,
114 SST, and others at $0.25^\circ \times 0.25^\circ$ and hourly resolution from the European Centre for Medium-Range Weather
115 Forecasts fifth generation reanalysis (ERA5) (Hersbach et al., 2019). RH_{SST} is estimated using ERA5 data: $RH_{SST} =$
116 e_{air}/e_{sat} , where e_{air} is vapor pressure of air and e_{sat} is saturation vapor pressure with respect to SST.
117 Additionally, precipitation data at $0.1^\circ \times 0.1^\circ$ and half-hourly resolution were obtained from the Integrated Multi-
118 satellitE Retrievals for GPM (V07) dataset (Huffman et al., 2023). Moreover, we used ERA5 data and
119 meteorological data at $1^\circ \times 1^\circ$ and 3-hourly resolution from the Global Data Assimilation System (GDAS) to
120 calculate backward trajectories (see Section 2.4 for details).

121 Statistical analyses primarily involved linear correlations and regressions, with the coefficient of determination
122 (R^2) used to quantify the variance explained by each variable. In addition, we also used composite analysis to reveal
123 relationships between variables. For example, to identify general patterns in backward trajectories associated with
124 d -excess exceeding 30‰, all the days with such high d -excess were compiled into a collection. A composite map of
125 trajectories from this collection was then constructed to reveal typical pathways under these conditions.

126 **2.3 Theoretical framework for the understanding of isotope compositions and humidity**

127 Besides complex atmospheric circulation models, the evolution of vapor isotope compositions during different
128 moistening and dehydration processes can be predicted through a compilation of atmospheric processes such as
129 condensation, mixing, and raindrop evaporation (Noone, 2012; Worden et al., 2007; Galewsky et al., 2016). These

130 process shape distinct pathways of isotopic evolution in relation to atmospheric humidity.

131 The Rayleigh distillation model describes the progressive condensation of water vapor (Dansgaard, 1964). The
132 isotope composition of remaining vapor, denoted as δ , can be expressed as $\delta = (1 + \delta_0)(q/q_0)^{\alpha-1} - 1$, where q
133 is the specific humidity, and α is the fractionation factor. A subscript of 0 refers to the initial condition of the air
134 mass. Raindrop evaporation introduces further complexity. As raindrops form at higher altitudes where vapor is
135 depleted in heavy isotopes, their partial evaporation affects the surrounding vapor, leading to isotope values lower
136 than those predicted by Rayleigh models (Risi et al., 2008a; Worden et al., 2007). This effect gives rise to “super-
137 Rayleigh” trajectories, characterized by an inflated effective fractionation factor (α_e), defined as $\alpha_e = (1 + \phi)\alpha$,
138 where ϕ quantifies deviations from equilibrium. Notably, Worden et al. (2007) and Noone (2012) have given
139 different equations for such deviations, and this study aligns with the formulations by Noone (2012).

140 Air mass mixing also influences humidity and isotopic compositions. When a dry air mass mixes with a moist
141 one, the specific humidity of the mixed air can be described as $q = f_{dry}q_{dry} + f_{moist}q_{moist}$, where f represents
142 the fraction of each air mass, with $f_{dry} + f_{moist} = 1$. Isotopic compositions are similarly derived by solving mass
143 balance equations for the light and heavy isotopes, resulting in a hyperbolic relationship between δ and q . In other
144 words, $\delta \times q$ and q should have a linear relationship in the mixing process (Fiorella et al., 2018). The intercept
145 of the regression between δ and $1/q$ or the slope between $\delta \times q$ and q provides an estimate of the moist end
146 member’s isotope composition (Keeling, 1958).

147 Assuming a surface temperature of 25 °C and relative humidity of 85%, we utilize the evaporation model by
148 Craig and Gordon (1965) to determine the isotopic composition of ocean evaporation. This results in $\delta^{18}\text{O} = -11.5\text{‰}$,
149 $\delta^2\text{H} = -81.4\text{‰}$, and $d\text{-excess} = 10.6\text{‰}$. These values serve as the wet end member for modeling moistening process
150 through mixing with ocean evaporation. For the dry end member, we consider a dehydrated air mass from the
151 Rayleigh curve at $q = 0.5 \text{ g/kg}$, $\delta^{18}\text{O} = -60.3\text{‰}$, and $\delta^2\text{H} = -418.0\text{‰}$ (Fig. S2). The dehydration process via

condensation is initiated at a relative humidity of 80% on the mixing line. Similarly, “super-Rayleigh” distillation involving partial rain evaporation also begins from this starting point. We explore two “super-Rayleigh” scenarios: Rain_evap_A assumes 2% rain evaporation, while Rain_evap_B assumes 5%, based on equations from Noone (2012). Additionally, we consider the influence of evapotranspiration over south Asia and the TP on atmospheric humidity and vapor isotope compositions over SETP. Quantifying isotopic compositions of land surface evapotranspiration is challenging. Given precipitation $\delta^{18}\text{O}$ over south Asia generally ranges from -1.0‰ to -5.0‰ (Bowen and Wilkinson, 2002; Terzer-Wassmuth et al., 2021) and transpiration constitutes two-thirds or more of evapotranspiration (Cao et al., 2022; Han et al., 2022; Good et al., 2015), we assume a $\delta^{18}\text{O}$ value of -5.0‰ as an upper bound for land surface evapotranspiration. Similarly, we assume a d -excess of 15.0‰ for this wet end member.

2.4 Backward trajectory and moisture source diagnostic

To investigate air mass transport and diagnose moisture sources and pathways toward SETP, we calculated backward trajectories using the Hybrid Single-Particle Lagrangian Integrated Trajectory model (HYSPLIT) (Stein et al., 2015). Trajectory calculations were driven by nested ERA5 (within the domain of 0-50°N and 40-120°E) and GDAS (globally but when outside of the ERA5 domain) data to achieve higher resolution in the major potential source regions. In addition, the vertical motion was also driven by the model vertical velocity. Air parcels were released from 5 locations: the study site and points displaced 0.2° in each cardinal direction. These releases occurred at 7 different vertical levels: 10, 50, 100, 200, 300, 400, and 500 m above ground level. For each day during the sampling campaign, trajectories were initiated every 3 hours to calculate 10-day backward trajectories, resulting in 280 trajectories per day. Geographical and meteorological variables, including location, pressure, temperature, specific humidity, rainfall amount, boundary layer height, and terrain height along the trajectories, were stored at hourly intervals.

To quantify moisture contributions along trajectories to SETP’s humidity, we applied the Lagrangian moisture

174 source diagnostic method developed by Sodemann et al. (2008). This method uses mass balance principles along
175 trajectories, interpreting increases in specific humidity (forward in time) as moisture uptake and decreases as
176 moisture loss due to precipitation. It also accounts for the reduced contribution of earlier moisture uptake due to
177 precipitation en route. We previously adapted this method to identify moisture sources for precipitation in sub-
178 regions of South Asia and East Asia (Cai et al., 2018; Cai and Tian, 2020).

179 In this framework, the moisture source can be attributed into four categories: contributions within an extended
180 boundary layer over 1) land and 2) ocean, 3) contributions from above the extended boundary layer, and 4)
181 remaining unattributed sources. Following Sodemann et al. (2008), the extended boundary layer was parameterized
182 as 1.5 times the boundary layer height. The diagnostic results indicated that approximately 7.0% of the moisture
183 arriving at SETP remained unattributed, confirming that 10-day trajectories are sufficient to diagnose most moisture
184 sources. Overall, the fractions of within-boundary-layer contributions are 60.2% over land and 5.0% over ocean,
185 with an additional 27.8% originating from above the extended boundary layer. Additionally, this study emphasizes
186 the contribution of air parcels themselves to SETP's humidity. This variable captures the history of the moisture and
187 indicates how much moisture within each air parcel finally reaches SETP.

188 The moisture contribution of an air parcel to SETP's humidity is a measure of the importance of upstream air.
189 We calculated weighted-mean values for key variables by using the moisture contribution of the air parcel along
190 trajectories as the weight. We also applied K-means clustering to group trajectories, helping to identify major
191 transport pathways. When calculating the mean trajectory for each cluster and meteorological variables along each
192 mean trajectory, the moisture contribution of the air parcel is also considered as the weight to calculate weighted-
193 means.

194 **3 Results**

195 **3.1 General characteristics of vapor $\delta^{18}\text{O}$, d -excess, and local meteorological variables**

196 Consistent with Yao et al. (2013), we defined June-September (JJAS) as the summer monsoon season. In
197 contrast, November-April (Nov-Apr) was designated as the non-monsoon season, with May and October considered
198 transition periods between the two seasons. In general, $\delta^{18}\text{O}$ values are at lower levels during the summer monsoon
199 season and higher levels during the non-monsoon season (Fig. 1a). Mean $\delta^{18}\text{O}$ values are -18.4‰ for the non-
200 monsoon season, -23.3‰ for the summer monsoon season, -16.9‰ for May, and -22.8‰ for October. $\delta^{18}\text{O}$ shows
201 a dramatic decrease at the onset of the summer monsoon. Conversely, from the end of the summer monsoon season
202 to spring and early summer, $\delta^{18}\text{O}$ shows a gradual increase trend. Although the amount effect significantly influences
203 this region, the seasonal variation of $\delta^{18}\text{O}$ does not strictly align with local precipitation patterns. For instance, while
204 local precipitation ceases clearly after the summer monsoon (Fig. 1e), $\delta^{18}\text{O}$ remains at relatively low levels. This
205 behavior is consistent with precipitation $\delta^{18}\text{O}$ in SETP, northeast India, and Bangladesh (Yao et al., 2013; Cai and
206 Tian, 2020; Yang et al., 2017).

207 Although d -excess values are also lower during the summer monsoon season and higher during non-monsoon
208 periods, the timing of seasonal transitions differs from that of $\delta^{18}\text{O}$ (Fig. 1b). Mean d -excess values are 18.3‰ for
209 the non-monsoon season, 11.9‰ for the summer monsoon season, 13.7‰ for May, and 14.9‰ for October. The
210 highest d -excess values generally occur during winter months when air temperature and relative humidity (RH) are
211 at their lowest levels (Fig. 1c and 1d). Furthermore, d -excess starts to decrease in spring, earlier than the sharp drop
212 in $\delta^{18}\text{O}$ at the onset of the summer monsoon.

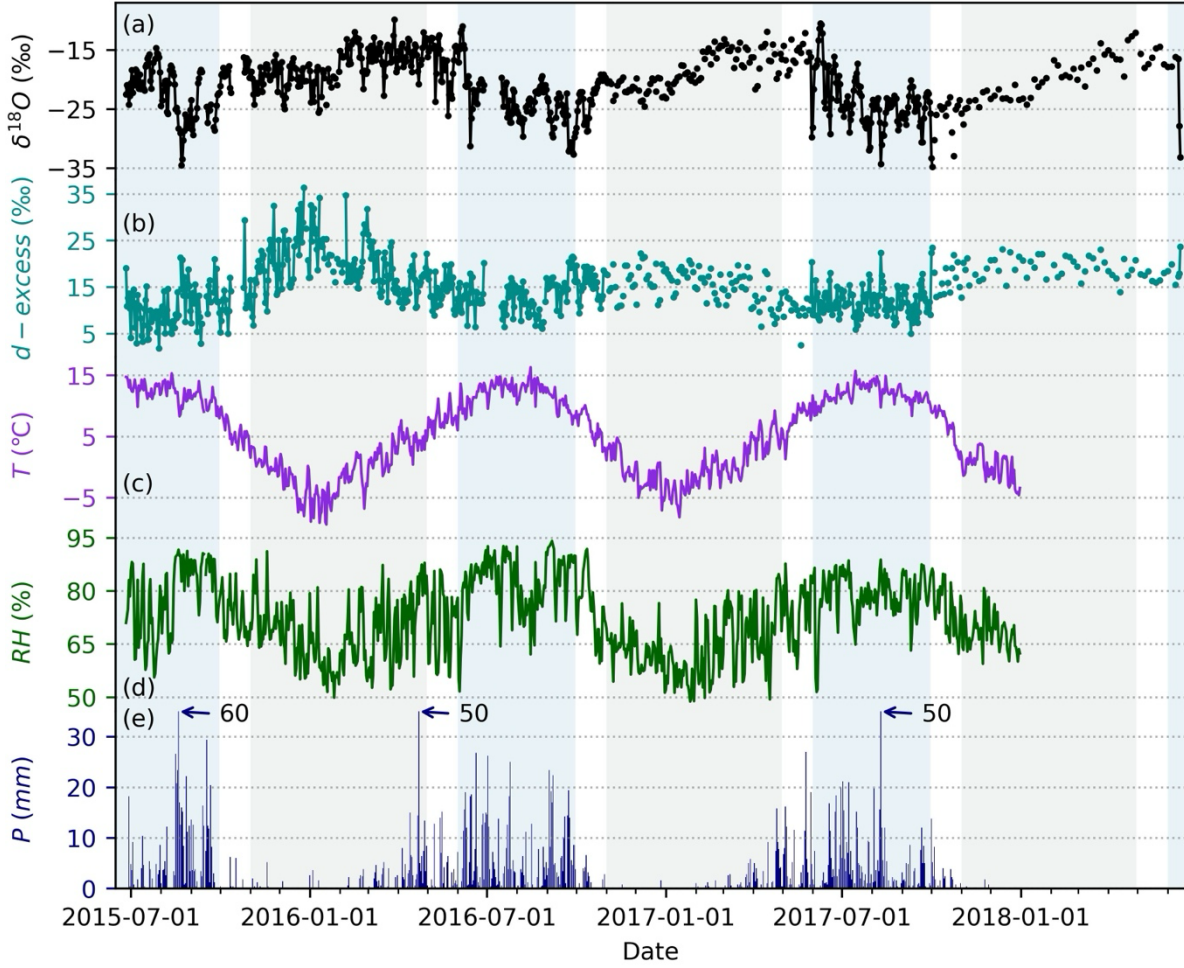
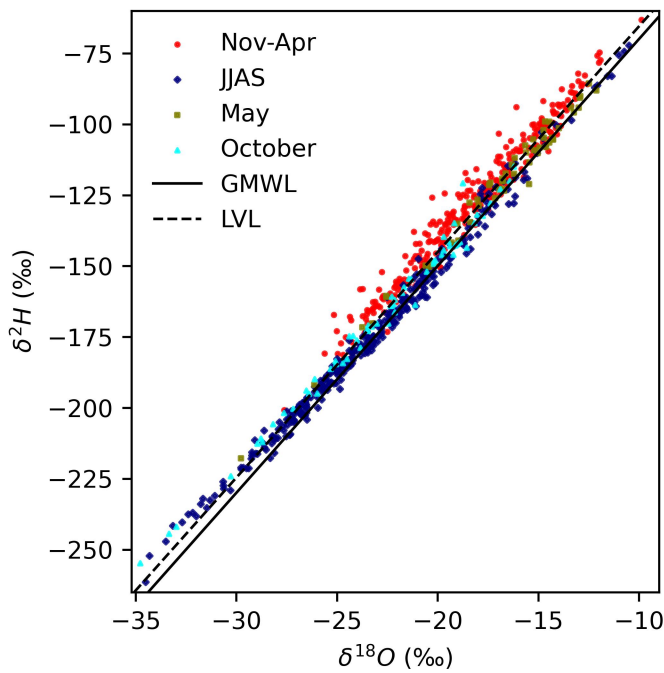


Figure 1. Time series of observed vapor $\delta^{18}\text{O}$, d -excess, and daily local meteorological variables from 2015-2018: (a) $\delta^{18}\text{O}$, (b) d -excess, (c) air temperature, (d) relative humidity (RH), and (e) precipitation amount. Light blue shading highlights the summer monsoon season, while light steel blue shading indicates the non-monsoon season.

The linear relationship between paired $\delta^{18}\text{O}$ and $\delta^2\text{H}$ values, along with their position relative to the global meteoric water line (GMWL, $\delta^2\text{H} = 8\delta^{18}\text{O} + 10$) (Craig, 1961), provides additional insights into isotopic fractionation processes (Putman et al., 2019). The local vapor line (LVL), estimated from all $\delta^2\text{H}$ and $\delta^{18}\text{O}$ data points, is $\delta^2\text{H} = 7.96\delta^{18}\text{O} + 14.04$ ($R^2 = 0.98$). This LVL plots above but approximately parallel with the GMWL. This relatively higher intercept of LVL reflects the continental location of the site and additional kinetic fractionation after ocean evaporation. The $\delta^2\text{H}$ - $\delta^{18}\text{O}$ relationship also varied seasonally. During the non-monsoon season, the LVL

224 is $\delta^2\text{H} = 7.58\delta^{18}\text{O} + 10.61$ ($R^2 = 0.96$), while during the summer monsoon season, it shifts to $\delta^2\text{H} = 7.53\delta^{18}\text{O} + 0.91$
 225 ($R^2 = 0.99$). Non-monsoon data primarily plot above both the GMWL and the overall LVL. Conversely, most
 226 monsoon season isotope data fall below the overall LVL, though the lowest δ -value points during this period are
 227 positioned above the overall LVL, suggesting additional kinetic fractionation such as rain evaporation (He et al.,
 228 2024). Vapor isotopes for May resemble those of the non-monsoon season but align more closely with both the
 229 GMWL and LVL, whereas data for October exhibit behaviors similar to the monsoon season observations.



230
 231 **Figure 2. Relationship between vapor $\delta^2\text{H}$ and $\delta^{18}\text{O}$. The data is presented for different seasons: non-**
 232 **monsoon (Nov-Apr) as red dots, summer monsoon (JJAS) as navy diamonds, May as olive squares, and**
 233 **October cyan triangles. The solid line indicates the global meteoric water line (GMWL). The dashed line**
 234 **indicates the local vapor line (LVL) estimated from all $\delta^2\text{H}$ and $\delta^{18}\text{O}$ data points.**

235 The relationships between $\delta^{18}\text{O}$ and specific humidity (q) further indicate distinct seasonal patterns in moisture
 236 dynamics (Fig. 3a). Due to unavailability of local meteorological data for 2018, our analyses focused on data
 237 collected before this year. During the non-monsoon season, particularly in winter months, most data points are
 238 positioned above the Rayleigh distillation line but below a mixing line that represents an upper bound of

239 hypothetical evapotranspiration over South Asia. This suggests a mix between a dry end member and a moist end
240 member. In contrast, during the summer monsoon season, data predominately fall below the Rayleigh line,
241 influenced by “super-Rayleigh” processes linked to rain evaporation.

242 Further insights come from examining $\delta \times q$ versus q relationships, which highlight seasonal contrasts in
243 moisture source signatures (Fig. S3). For the non-monsoon season, a simple estimation through the linear regression
244 between $\delta \times q$ and q suggests a moist end member with an $\delta^{18}\text{O}$ of $-13.9\text{‰} \pm 0.6\text{‰}$. The amount weighted annual
245 mean precipitation $\delta^{18}\text{O}$ at our site was about -14.5‰ (Yao et al., 2013). However, during the monsoon season, the
246 overall estimation of $\delta^{18}\text{O}$ for the moist end member through the linear regression between $\delta \times q$ and q is
247 significantly lower at $-30.9\text{‰} \pm 1.8\text{‰}$, pointing to an additional moisture source from rain evaporation that is more
248 depleted in heavy isotopes. These results align with the distribution of $\delta^{18}\text{O}$ - q data below the Rayleigh line during
249 the summer monsoon season (Fig. 3a), underscoring the influence of different moisture sources and processes across
250 seasons.

251 The relationships between d -excess and q also reflect seasonal contrasts in moisture dynamics (Fig. 3b). During
252 non-monsoon season months, a negative correlation is observed where lower q corresponds to higher d -excess
253 values (Figs. 1 and 3b). This relationship is particularly pronounced under dry and cold conditions. In contrast,
254 during the summer monsoon season, no clear relationship between d -excess and q is apparent, with d -excess
255 showing considerable variability of approximately 20‰ at any given q . These findings suggest that d -excess is less
256 predictable using q compared to $\delta^{18}\text{O}$, except under low humidity levels.

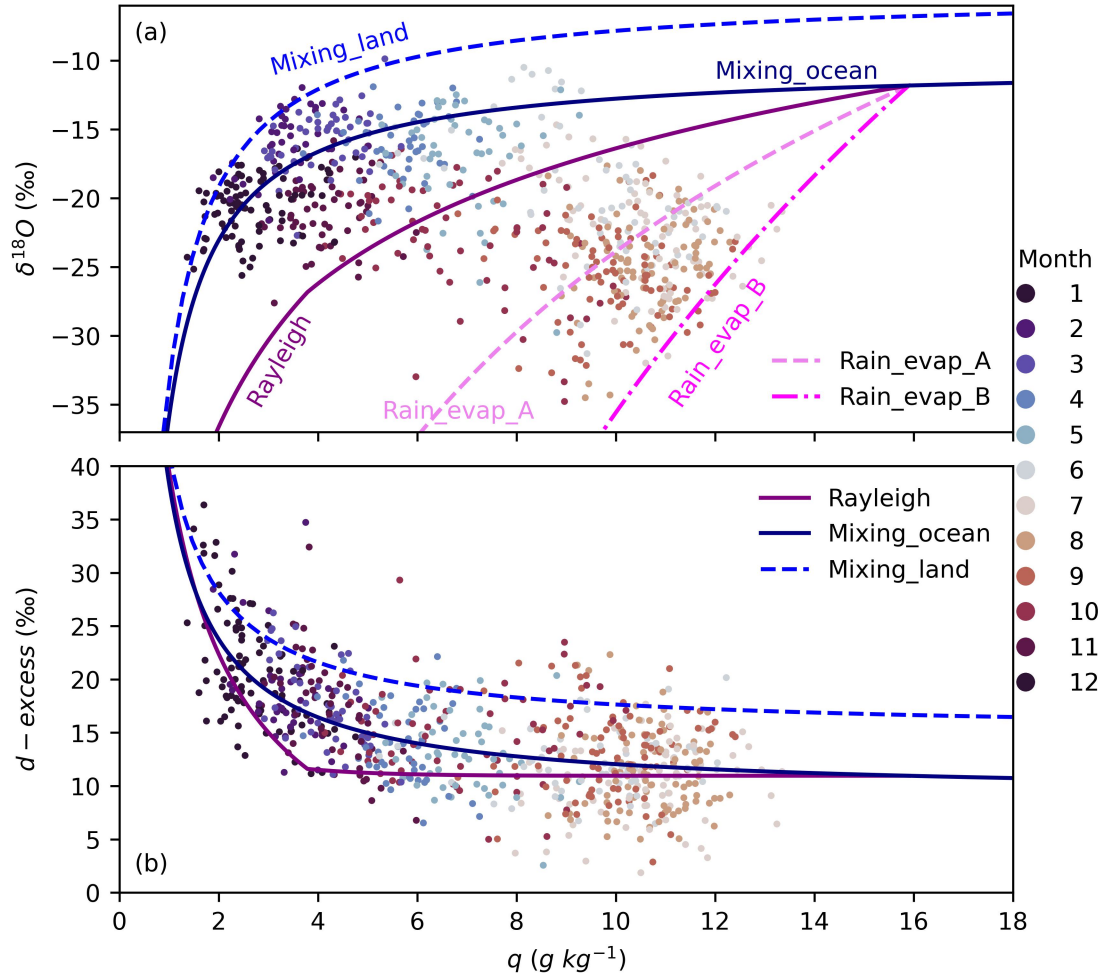


Figure 3. Relationships between vapor isotopes ($\delta^{18}\text{O}$ and $d\text{-excess}$) and specific humidity (q) from 2015-2017. (a) scatter plot of $\delta^{18}\text{O}$ against q . (b) scatter plot of $d\text{-excess}$ against q . Each data point is color-coded by month. Reference lines correspond to those in Fig. S2; their interpretations are detailed in Fig. S2 and Section 2.3. Note that only data before 2018 are shown (see text for details).

3.2 Seasonal variability in moisture sources and transport pathways

To understand the drivers behind the seasonal variations in moisture dynamics, we analyzed the moisture sources and transport pathways during different seasons (Fig. 4). Our focus was on the contribution of moisture from historical air masses (last 10 days) to humidity at SETP.

During the non-monsoon season (Fig. 4a), moisture is mainly transported via two pathways: one originating from the west of SETP, carried by the westerlies (clusters Nov-Apr2 and Nov-Apr3), and another from the south,

268 such as the BOB (cluster Nov-Apr1). Quantitatively, the contribution is 84.8% from the southern pathway and 15.2%
269 from the western branches combined. Interestingly, when considering only trajectories without accounting for
270 moisture contributions, all three clusters appear to originate from the west or southwest of SETP (Fig. S4). This
271 discrepancy highlights the importance of distinguishing between pure air mass transport and actual moisture sources
272 when interpreting trajectory data.

273 In contrast, during the summer monsoon season (Fig. 4b), moisture transport is predominantly from the south
274 of SETP, driven by the summer monsoon. The pathways observed in May (Fig. 4c) represent a transition from the
275 non-monsoon season (Fig. 4a) toward the dominant southerly transport seen during the summer monsoon (Fig. 4b).
276 In comparison, the moisture sources and transport pathways exhibit a slight eastward shift during October compared
277 with those during the summer monsoon season (Figs. 4d and S4d).

278 Another notable aspect of the moisture source distributions is the dominant contribution from proximal
279 terrestrial regions, particularly those to the south of SETP (Fig. 4). For example, the 1% contour representing
280 moisture contributions from air parcels over each $1^\circ \times 1^\circ$ grid box does not or barely extend into oceanic regions
281 during any of the four seasons. This indicates that surface evaporation from oceanic regions such as the BOB and
282 AS contributes minimally. Quantitatively, the within-boundary-layer contributions from oceanic regions are
283 determined to be 2.5%, 9.1%, 4.6%, and 2.0% for non-monsoon, summer monsoon, May, and October, respectively.
284 Most of the moisture originating over these oceanic regions is lost through precipitation before reaching SETP, and
285 what remains is replenished by evapotranspiration during transport over land. This finding raises an important
286 question: do the vapor isotopes measured at SETP still reflect the meteorological conditions at their oceanic sources?

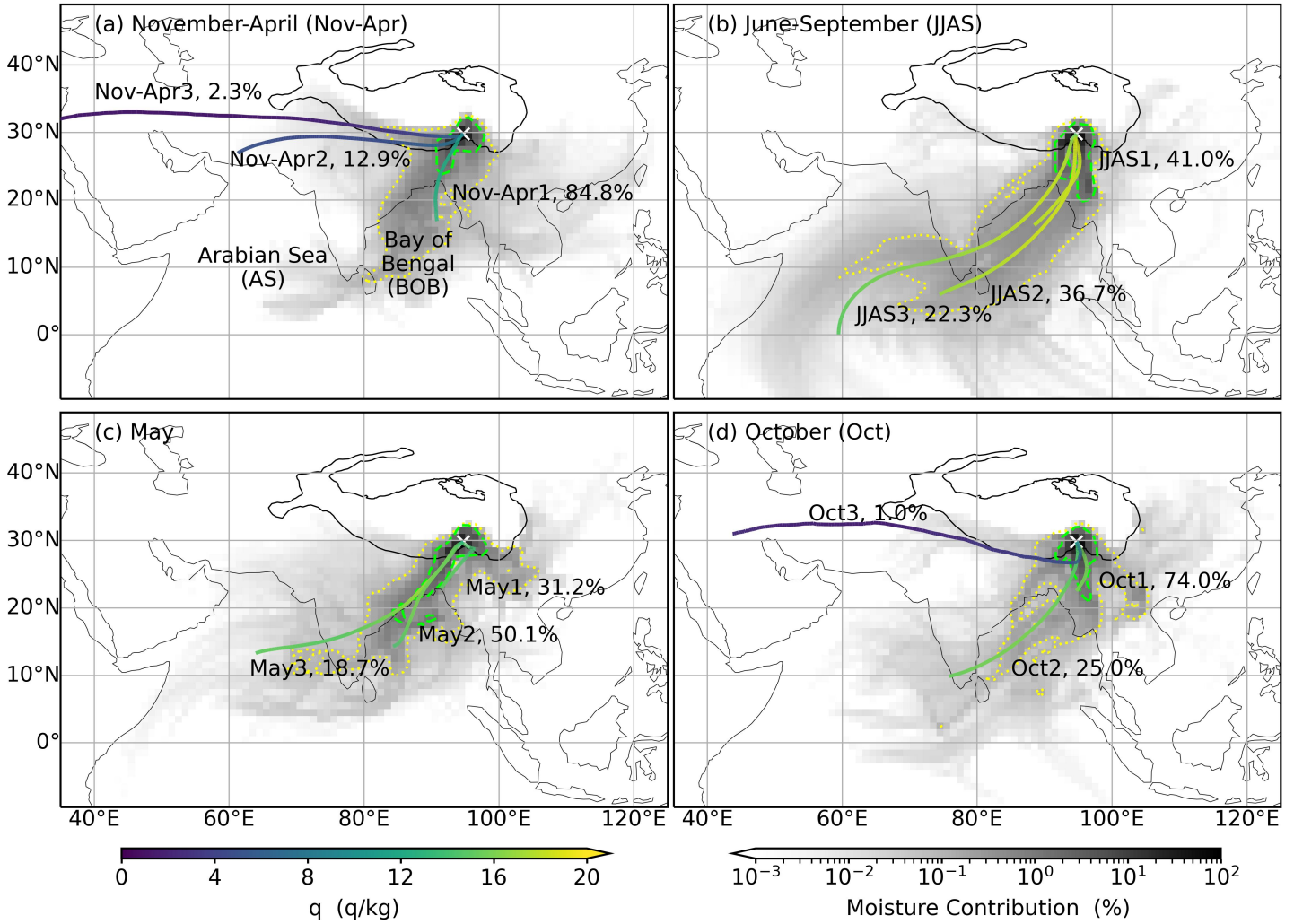


Figure 4. Moisture sources and transport pathways during different seasons from 2015-2017. (a) spatial distribution of relative contributions of moisture from all air parcels over each $1^{\circ} \times 1^{\circ}$ box (shading) to humidity at the SETP station, along with specific humidity (q) along mean trajectories (weighted by moisture contributions) for the non-monsoon season of November-April (Nov-Apr). (b-d) are the same as (a), but for the monsoon season of June-September (JJAS, b), May (c), and October (d), respectively. The dotted yellow and dashed green contours indicate the moisture contribution at 0.1% and 1%, respectively. The yellow crosses indicate the location of the SETP station. The black solid lines denote the Tibetan Plateau with altitude contour at 3000 m.

3.3 Role of ocean surface evaporation conditions at seasonal and intraseasonal time scales

Relationships between d -excess and ocean surface evaporation conditions, such as RH_{SST} and SST, were examined using data from 2015-2017 (Fig. 5a and Fig. S5a). Results indeed show negative correlations between d -excess and RH_{SST} over northern Indian Ocean, particularly in the northern parts of AS and BOB (Fig. 5a). Specifically, the regression slopes for this relationship across the northern Indian Ocean vary from higher than $-0.1\text{‰} \text{‰}^{-1}$ to values below $-0.6\text{‰} \text{‰}^{-1}$.

Focusing on specific regions, the northern BOB ($10\text{--}22^{\circ}\text{N}$ and $80\text{--}99^{\circ}\text{E}$) and the eastern AS ($7\text{--}20^{\circ}\text{N}$ and $65\text{--}78^{\circ}\text{E}$; Fig. 5a) exhibited regression slopes within the range (from $-0.3\text{‰} \text{‰}^{-1}$ to $-0.6\text{‰} \text{‰}^{-1}$) previously reported (Uemura et al., 2008; Benetti et al., 2014; Liu et al., 2014; Bonne et al., 2019). For instance, the regional average RH_{SST} in the eastern AS shows an overall regression slope of $-0.49\text{‰} \text{‰}^{-1}$ ($r = -0.52$ and $p < 0.01$) (Fig. 6a), while the northern BOB has a slope of $-0.52\text{‰} \text{‰}^{-1}$ ($r = -0.55$ and $p < 0.01$) (Fig. 6b). However, the clustering of data points by season (Fig. 6) suggests that the apparent negative correlations might primarily stem from opposing seasonal trends. Similarly, apparent negative correlations between d -excess and SST also emerge over the northern Indian Ocean (Fig. S5a). Yet, both theoretical prediction (Merlivat and Jouzel, 1979) and in-situ observations above the ocean surface (Bonne et al., 2019; Liu et al., 2014) reveal a positive correlation between d -excess and SST. These discrepancies lead us to speculate that the overall correlations between SETP vapor d -excess and surface evaporation conditions over the northern Indian Ocean are likely driven by seasonal variability.

The relationship between d -excess and RH_{SST} was further analyzed by distinguishing between the summer monsoon and non-monsoon seasons. During the summer monsoon season, the negative correlation diminishes significantly, with correlation coefficients dropping below 0.3 (Fig. 5b). In contrast, significant correlations present during the non-monsoon season (Fig. 5c), potentially due to intraseasonal variations where d -excess peaks in winter and decreases at the beginning and ending of the non-monsoon season (Fig. 1b), possibly accompanied by opposing

317 RH_{SST} trends. Although the correlation is significant during the non-monsoon season, the explained variance in d -
318 excess remains low, at a maximum of 10%-16% over the northern BOB. Similarly, correlations with SST over the
319 northern Indian Ocean also become negligible when seasons are considered separately (Fig. S5). To account for
320 transport time, we examined correlations between d -excess and RH_{SST} from 1 to 11 days prior to the d -excess
321 observation dates during the summer monsoon (Fig. S6) and non-monsoon seasons (Fig. S7), respectively. The
322 results are consistent with those shown in Fig. 5, indicating that considering these lagged timeframes does not
323 enhance the correlation between d -excess and RH_{SST} . In summary, vapor d -excess at SETP is less likely a
324 conservative tracer of surface evaporation conditions (neither RH_{SST} nor SST) over the northern Indian Ocean.
325 Therefore, interpreting d -excess in meteoric water or paleo archives from the TP as a proxy for Indian Ocean
326 evaporation conditions should be approached with caution.

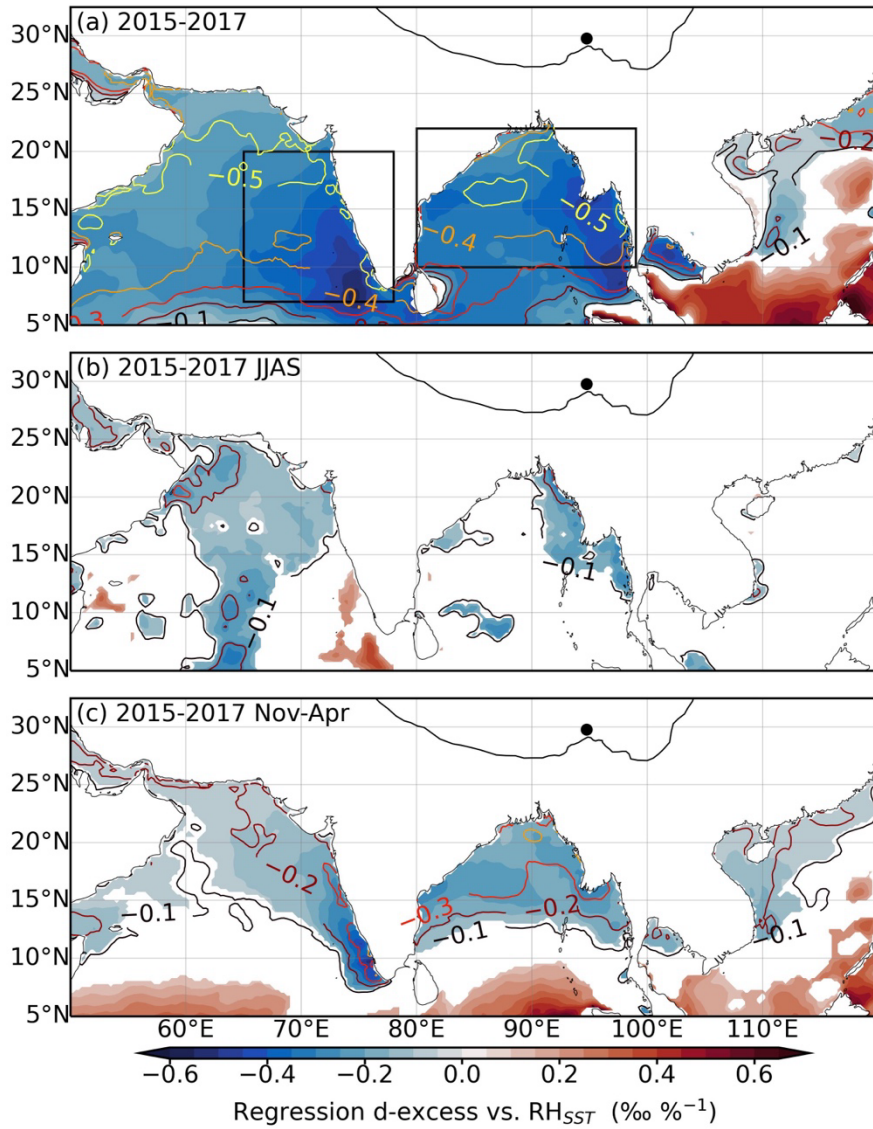


Figure 5. Relationships between vapor d -excess and relative humidity scaled to sea surface temperature (RH_{SST}). (a) regression of d -excess against RH_{SST} (shading and only values significant at the 95% significance level are shown) and correlation coefficients between them (contours at an interval of 0.1 and only negative correlations are shown) for all the data from 2015-2017. (b) and (c) are the same as (a) but only for the data within the summer monsoon season (JJAS) or the non-monsoon season (Nov-Apr), respectively. The black dots indicate the location of the SETP station. The black solid lines denote the Tibetan Plateau with altitude contour at 3000 m.

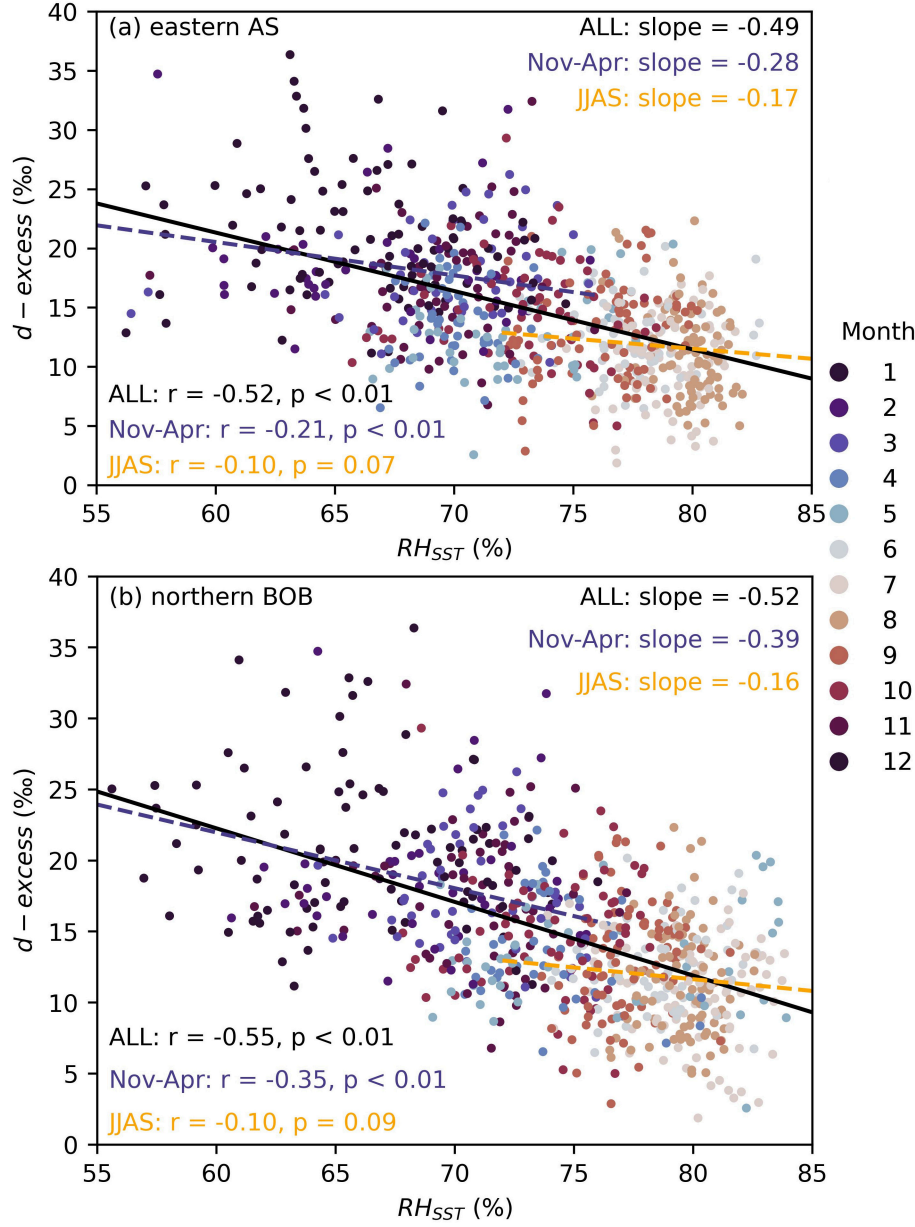


Figure 6. Relationships between SETP vapor d -excess and relative humidity normalized to sea surface temperature (RH_{SST}) averaged over (a) eastern Arabian Sea (7-20°N and 65-78°E) and (b) Bay of Bengal (10-22°N and 80-99°E) from 2015-2017. Each data point is color-coded by month. Solid black lines indicate the linear regression between all data points. Dashed orange lines indicate linear regression for data during the non-monsoon season (Nov-Apr) and dashed dark blue lines for data during the summer monsoon (JJAS). The slope (‰ %⁻¹), r , and p values for the three data groups are also shown.

342 3.4 Role of dry and cold air intrusion during the non-monsoon season

343 Both theoretical predictions from the Rayleigh model and observations during the non-monsoon season suggest
344 that d -excess increases as q decreases when q reaches extremely low values (Fig. 2). In addition, results for both air
345 mass transport and moisture transport show the significant role of the westerlies (Figs. S4a and 4a). Based on these
346 evidences, we propose that during the non-monsoon season, vapor isotopes are influenced by the mixing of cold
347 and dry air transported by westerlies from higher altitudes with surface vapor. Furthermore, surface vapor influenced
348 by recycled moisture from terrestrial evapotranspiration would further elevate d -excess at a given q (Fig. 3b).

349 We performed a composite analysis on moisture sources and transport pathways for the highest (higher than
350 30‰, and $n = 10$) and lowest (lower than 10‰, and $n = 8$) d -excess observations during the non-monsoon season
351 (Fig. 7). High d -excess values are primarily associated with moisture transported by westerlies from regions west
352 or southwest of SETP, such as over the TP and northern India. In addition, backward trajectories for these cases
353 show air masses characterized by extremely low q , reaching below 2 g kg^{-1} along the mean trajectories (weighted
354 by moisture contribution) over the TP (Fig. 7a). Conversely, for low d -excess cases, the moisture transport pathways
355 shift toward more humid regions south of SETP, including northeast India, Bangladesh, and the BOB (Fig. 7b). This
356 contrasting moisture transport pattern between high and low d -excess cases aligns with our hypothesis that high d -
357 excess is associated with dry and cold air transported by westerlies.

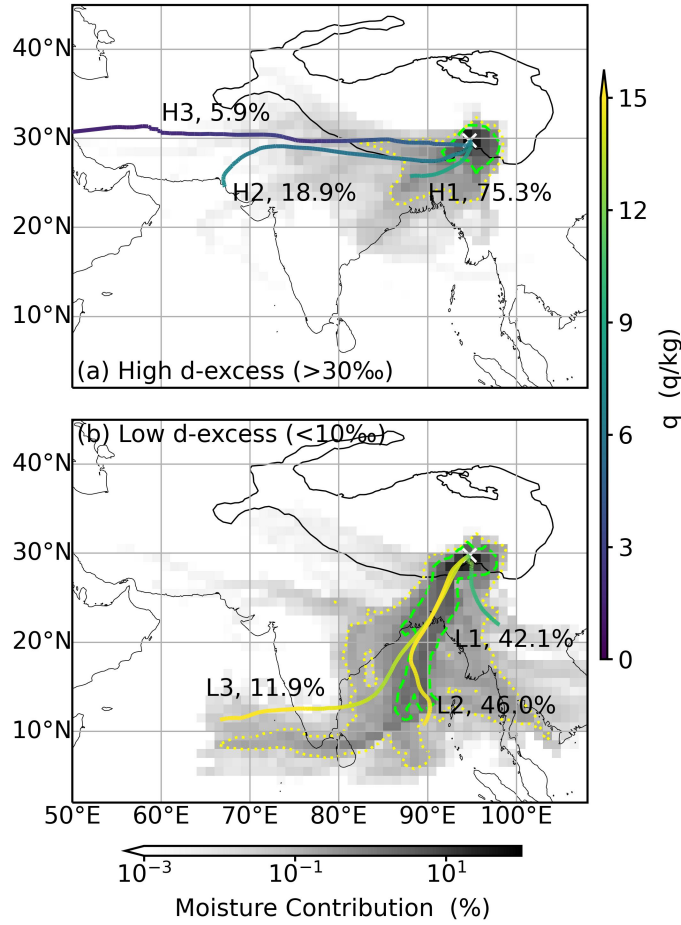


Figure 7. Composite of moisture sources and transport pathways for high and low d -excess days during the non-monsoon season of November-April. (a) spatial distribution of relative contribution of moisture from all air parcels over each $1^\circ \times 1^\circ$ box (shading) to humidity at the SETP station, along with specific humidity (q) along mean trajectories (weighted by moisture contributions) for d -excess values higher than 30‰ during the non-monsoon season ($n = 10$). (b) is the same as (a) but for d -excess lower than 10‰ ($n = 8$). The yellow crosses indicate the location of the SETP station. The black solid lines denote the Tibetan Plateau with altitude contour at 3000 m.

The influence of cold and dry air intrusions was further investigated through an analysis of relationships involving d -excess, local q , weighted-mean upstream q , weighted-mean upstream air temperature, and weighted-mean upstream air altitude (Fig. 8). Upstream variables represent weighted averages along the 10-day backward trajectory, where weights correspond to the moisture contribution at each time step (Section 2.4). The non-monsoon

370 season d -excess shows robust negative correlations with both local q ($r = -0.65$, $p < 0.01$; Fig. 8a) and upstream q
 371 ($r = -0.48$, $p < 0.01$). Furthermore, local q is strongly linked with upstream q ($r = 0.83$, $p < 0.01$; Fig. 8b), which is
 372 associated with air masses characterized by low temperatures and high altitudes (Figs. 8c and 8d). Additionally, the
 373 properties of the upstream air could also impact $\delta^{18}\text{O}$. Indeed, $\delta^{18}\text{O}$ during high d -excess cases is lower than during
 374 low d -excess cases (at a significance level of 95.3%). The overall correlation coefficient between $\delta^{18}\text{O}$ and d -excess
 375 during the non-monsoon season is -0.29 ($p < 0.01$). Notably, correlations between $\delta^{18}\text{O}$ and q are weaker compared
 376 to those observed for d -excess, with local q showing $r = 0.42$ ($p < 0.01$) and upstream q showing $r = 0.41$ ($p < 0.01$).
 377 The relationship between non-monsoon season $\delta^{18}\text{O}$ and humidity is mainly expressed as the relationship between
 378 $\delta \times q$ and q ($r = 0.82$ for local q and $r = 0.80$ for upstream q). Spatial correlations between vapor isotopes ($\delta^{18}\text{O}$
 379 and d -excess) and 2-meter air temperature as well as humidity measured by 2-meter dew point temperature also
 380 support these findings (Fig. S8). Significant negative correlations between d -excess and dew point temperature exist
 381 over southeastern TP, northeast India, and northern Bangladesh. In contrast, $\delta^{18}\text{O}$ shows significant positive
 382 correlations with air temperature over the India subcontinent and northwestern Southeast Asia.

383 As shown in Fig. 3b, extremely high d -excess values are predicted at very low q levels. Previous studies have
 384 shown that as q approaches zero, vapor d -excess can approach 7000‰ following the Rayleigh distillation trajectory
 385 (Bony et al., 2008), a behavior inherent to the definition of d -excess (Dütsch et al., 2017). High d -excess values
 386 have also been observed in low humidity environments, like polar regions (Bonne et al., 2014; Steen-Larsen et al.,
 387 2017) and high altitudes (Samuels - Crow et al., 2014; Sodemann et al., 2017; Webster and Heymsfield, 2003).
 388 Therefore, we infer that the increasing trend of d -excess with decreasing local q , upstream q , and regional dew point
 389 temperature is due to enhanced mixing with dry and cold subsiding air transported by westerlies from high altitudes.
 390 Relationships between upstream q and upstream air temperature as well as altitude further support this inference,
 391 indicating that low humidity conditions are associated with the presence of subsiding dry and cold air from high

altitudes (Figs. 8c and 8d). Therefore, vapor d -excess during the non-monsoon not only provides insights into specific humidity levels but also indicates the source of humidity.

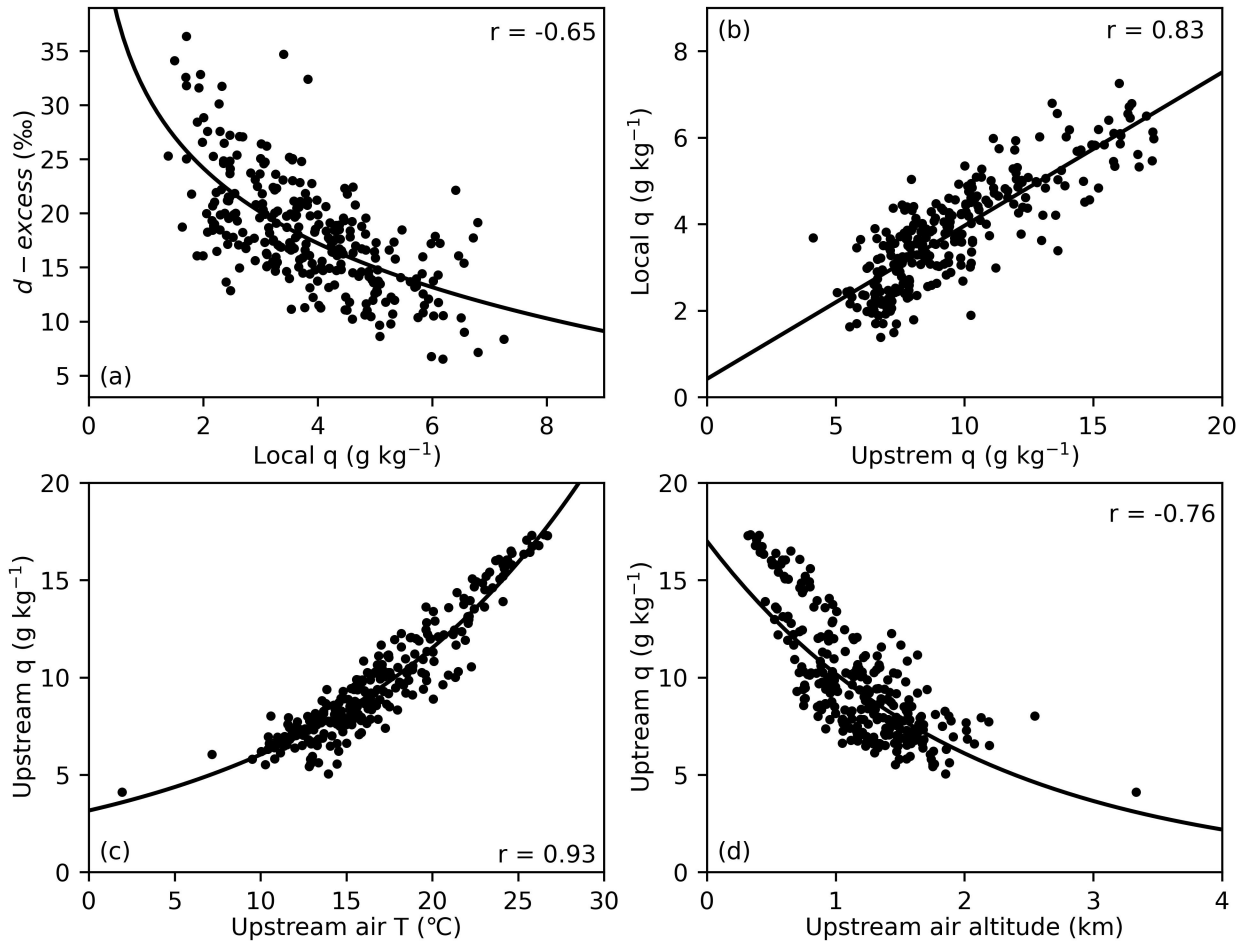


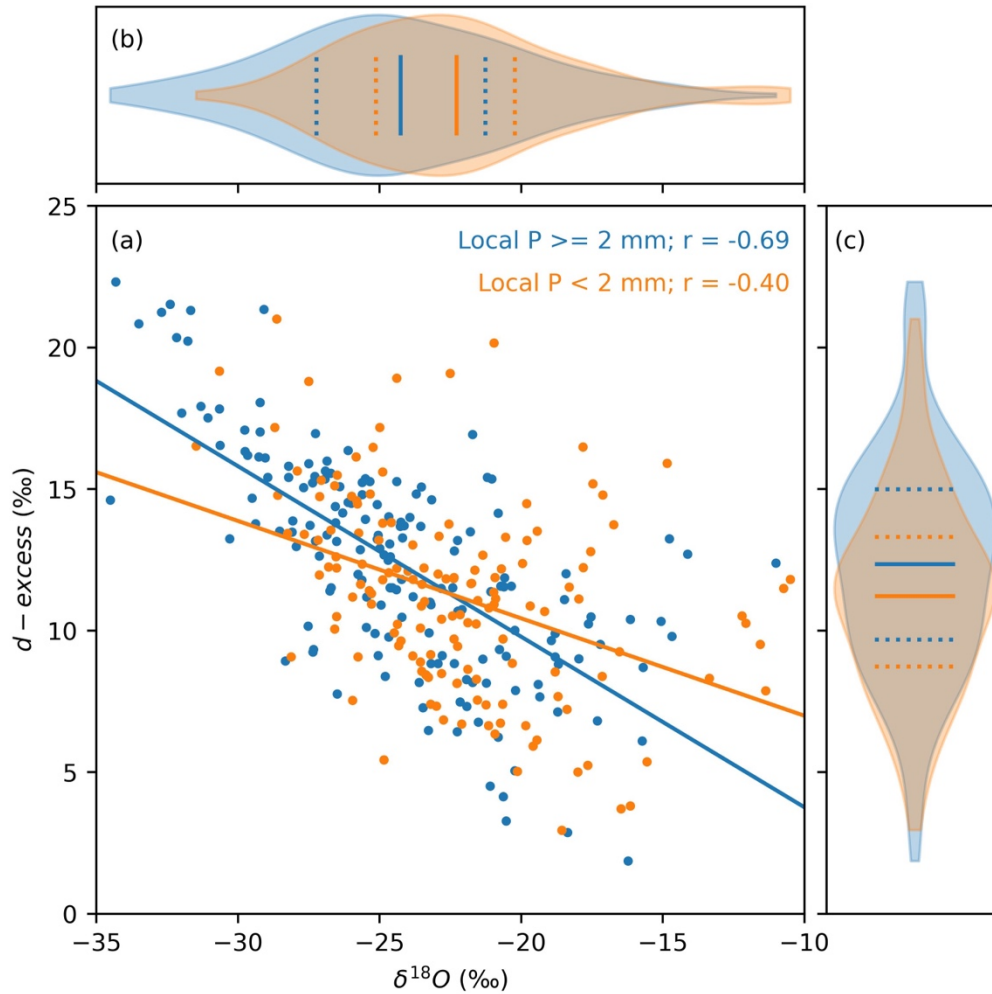
Figure 8. Relationships among vapor d -excess, local specific humidity (q), weighted-mean upstream q , weighted-mean upstream air temperature (T), and weighted-mean upstream air altitude during the non-monsoon season of November-April. (a) scatter plot of d -excess against local q . (b) scatter plot of local q against upstream weighted-mean q . (c) scatter plot of upstream q against upstream air T . (d) scatter plot of upstream q against upstream air altitude. All the upstream variables are mean values along backward trajectories weighted by the moisture contribution of air parcels. The solid curves indicate the log (a, c, and d) or linear (b) regression between the respective variables with the correlation coefficients indicated by the numbers.

3.5 Role of rain-vapor interaction during the summer monsoon season

In contrast to the significant dependence of d -excess on q during the non-monsoon season, no correlation is observed ($r = 0.04$, $p = 0.51$) during the summer monsoon season. The behavior of $\delta^{18}\text{O}$ also differs between the two seasons (Fig. 3). During the summer monsoon season, $\delta^{18}\text{O}$ - q plots below the Rayleigh curve, indicating that the vapor has experienced rain-vapor interaction through rain evaporation (Fig. 3a). Partial rain evaporation in an unsaturated atmospheric environment leads to kinetic fractionation, which decreases d -excess values in raindrops while increasing d -excess in the surrounding vapor (Risi et al., 2008b). This effect of rain-vapor interaction on vapor isotopes has been suggested as a primary mechanism driving the amount effect in tropical regions (Risi et al., 2008a; Kurita et al., 2011; Bowen et al., 2019; Galewsky et al., 2016). Therefore, we hypothesize that vapor isotopes during the summer monsoon season at SETP are influenced by the extent of rain-vapor interaction.

The first evidence supporting this hypothesis is the significant correlation between $\delta^{18}\text{O}$ and d -excess during the summer monsoon season ($r = -0.55$, $p < 0.01$; Fig. 9a). In addition, $\delta^{18}\text{O}$ and d -excess show a trend of weak correlation at high $\delta^{18}\text{O}$ values, but a stronger correlation when $\delta^{18}\text{O}$ values are low (Figs. 9a and S9). To explore this further, we categorized days with daily precipitation of at least 2 mm as “rainy days” and those with less than 2 mm as “non-rainy days”. This distinction is based on the premise that rain-vapor interaction cannot occur in the absence of rainfall. The analysis reveals that $\delta^{18}\text{O}$ during rainy days is significantly lower than that during non-rainy days, while d -excess show the opposite trend ($p < 0.01$ for both $\delta^{18}\text{O}$ and d -excess; Figs. 9b and 9c). Furthermore, the correlation between $\delta^{18}\text{O}$ and d -excess becomes stronger on rainy days ($r = -0.69$, $p < 0.01$), though a weaker negative correlation persists even on non-rainy days ($r = -0.40$, $p < 0.01$). Even when applying a stricter threshold of 0 mm for non-rainy days, the negative correlation between $\delta^{18}\text{O}$ and d -excess remains significant ($r = -0.37$, $p < 0.01$). Moreover, correlations with local precipitation amount are weak for both $\delta^{18}\text{O}$ ($r = -0.31$, $p < 0.01$) and d -excess ($r = 0.26$, $p < 0.01$). These findings lead us to infer that vapor isotopes during the summer monsoon season

425 at SETP are influenced not only by local rain-vapor interactions but also by the history of rain-vapor interactions
 426 that occurred before the vapor reached the region.



427
 428 **Figure 9. Relationships between SETP vapor $d\text{-excess}$ and $\delta^{18}\text{O}$ during the summer monsoon season. (a)**
 429 **scatter plot of $d\text{-excess}$ against $\delta^{18}\text{O}$ and linear regression lines between them. (b) distribution of $\delta^{18}\text{O}$ values**
 430 **with the dashed lines indicate values at the lower and upper quartiles and the solid lines indicate the mean**
 431 **values. (c) is the same as (b) but for $d\text{-excess}$. Orange colors indicate data observed during daily precipitation**
 432 **amount less than 2 mm and blue colors indicate data observed during days with precipitation amount not**
 433 **less than 2 mm. The r values for both lines are indicated in (a) and both are significant at the 0.01 level.**

434 To further investigate the role of rain-vapor interactions, we use total precipitation amount (P_{acc}) as an indicator
 435 of rain-vapor interaction, considering the cumulative effect over several days preceding sampling. Our analysis

436 examined correlations between vapor isotopes ($\delta^{18}\text{O}$ and d -excess) and P_{acc} over periods ranging from 1-10 days
437 prior to sampling (Figs. S10 and S11). Vapor d -excess reaches an optimal correlation with P_{acc} when considering 3
438 days before sampling (P_{acc_3d}). Vapor $\delta^{18}\text{O}$ shows a slightly longer memory and reaches an optimal correlation
439 around 5-6 days before sampling. Figure 10 shows the spatial distribution of these correlations, where d -excess
440 positively correlates with P_{acc_3d} across a $\sim 5^\circ \times 5^\circ$ region surrounding SETP and extending southwestward to the
441 Himalayas (Fig. 10a). In contrast, $\delta^{18}\text{O}$ shows significant negative correlations in similar regions (Fig. 10b).
442 Interestingly, even on non-rainy days, significant regional-scale correlations persist, albeit weaker and with a smaller
443 spatial extent (Fig. S12).

444 These findings provide further insights into understanding the mechanisms driving the amount effect. The
445 negative correlation between $\delta^{18}\text{O}$ and P_{acc} has also been observed in precipitation and can be attributed to either
446 continuous rainout (Ruan et al., 2019; Kurita et al., 2015; Cai and Tian, 2016) or rain-vapor interactions (Lawrence
447 et al., 2004; Risi et al., 2008a; Kurita et al., 2011; Worden et al., 2007). While continuous rainout, explained by the
448 Rayleigh distillation model, accounts for the decreasing trend of $\delta^{18}\text{O}$ with increased rainfall, d -excess remains
449 relatively stable unless specific humidity drops to very low levels ($\sim 4 \text{ g kg}^{-1}$ in Fig. 3b for example). The positive
450 correlation between vapor d -excess and P_{acc_3d} provides an additional constraint, suggesting that the amount effect
451 is not solely a result of rainout but also involves rain-vapor interactions, which significantly influence vapor isotopes
452 in the lower troposphere.

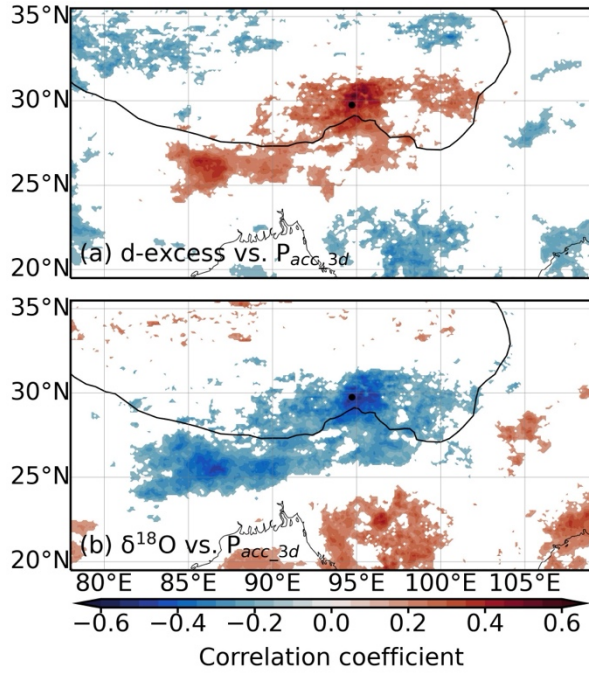


Figure 10. Relationships between vapor isotopes for rainy days (local daily precipitation amount not less than 2 mm) and total precipitation amount at the regional scale during the summer monsoon season. (a) spatial distribution of correlation coefficients between d -excess and total precipitation amount during 3 days prior sampling (P_{acc_3d}). (b) is the same as (a) but for $\delta^{18}O$. Only values significant at the 95% significance level are shown. The black dots indicate the location of the SETP station. The black solid lines denote the Tibetan Plateau with altitude contour at 3000 m.

4 Implications for interpreting TP ice core isotope data

Interpreting d -excess in meteoric water and ice cores on the TP is complicated by evaporation conditions over the northern Indian Ocean (RH_{SST} and SST) and continental recycling (Shao et al., 2021; Zhao et al., 2012; Joswiak et al., 2013; Pang et al., 2012; An et al., 2017). Attempts have been made to establish relationships between vapor d -excess and RH_{SST} (Chen et al., 2024; Liu et al., 2024), as well as between ice core d -excess and RH_{SST} (Shao et al., 2021) or SST (Zhao et al., 2012). Based on our results (Section 3.3), however, the apparent relationships are primarily a result of similarities in the seasonality of these variables. The preservation of oceanic source region

467 conditions by vapor *d*-excess have also been questioned at other continental sites (Fiorella et al., 2018; Aemisegger
468 et al., 2014; Welp et al., 2012; Wei and Lee, 2019; Samuels - Crow et al., 2014). Instead, these studies emphasized
469 the role of other processes, such as continental recycling and mixing with subsiding air masses.

470 The direct contribution of oceanic vapor to humidity at SETP is very limited (Fig. 4), implying an even smaller
471 contribution over the TP since SETP is at the forefront of moisture transport toward TP (Fig. S1). The dominant
472 terrestrial origin indicates significant continental recycling. Terrestrial processes such as transpiration and
473 evaporation introduce isotopically enriched moisture with high *d*-excess signatures. Interestingly, vapor $\delta^{18}\text{O}$
474 exhibits a noticeable positive correlation with the fraction of within-boundary-layer moisture contribution over land
475 during the non-monsoon season ($r = 0.47$, $p < 0.01$), supporting that enhanced continental recycling would elevate
476 $\delta^{18}\text{O}$ values (Fig. 3a). However, correlations between the fraction of terrestrial moisture source and $\delta^{18}\text{O}$ for other
477 seasons or with *d*-excess are either insignificant or marginal (Table S1). Further quantification of the effect of
478 continental recycling on vapor isotopes requires detailed knowledge of the isotope compositions of
479 evapotranspiration fluxes. In this study, we utilized a simplified assumption regarding the isotopic composition of
480 these fluxes to explore their influence on vapor isotopes. Therefore, future research should prioritize characterizing
481 the isotopic signatures of both evaporation and transpiration fluxes, as well as determining the ratio between these
482 two fluxes. This will provide deeper insights into how continental recycling shapes vapor isotope compositions.

483 Seasonal changes and long-term variations in precipitation and ice core isotopes have been interpreted as shifts
484 in moisture source between recycled terrestrial moisture and oceanic sources or their relative contributions (An et
485 al., 2017; Yang and Yao, 2020). Oceanic moisture is typically associated with the summer monsoon, while westerlies
486 bring moisture from continental recycling or even the Mediterranean Sea. Water isotope signatures on the TP were
487 thought to reflect this interplay between the summer monsoon and non-monsoon seasons (Joswiak et al., 2013; Pang
488 et al., 2012; Tian et al., 2007). Despite seasonal shifts in moisture sources, continental recycling prevails throughout

the year (Fig. 4). Our alternative perspective explains high d -excess induced by westerlies as dry and cold air intrusions rather than surface evaporation or evapotranspiration. While the interplay between the summer monsoon and westerlies remains valid, but we emphasize changes in air mass properties driven by different circulation systems.

The proposed alternative interpretation aligns with findings from the Andes (Samuels - Crow et al., 2014) and Corsica (Sodemann et al., 2017), potentially offering an explanation for the abnormally high d -excess in high-altitude ice cores, as mentioned in the Introduction. This is because specific humidity at these ice core sites is extremely low, and prolonged interaction with cold and dry air may further modify snow isotope compositions (Ma et al., 2024; Wahl et al., 2022). In addition, intense rain-vapor interactions during the summer monsoon represent another potential source of elevated d -excess (Section 3.5). When this high d -excess vapor contributes to subsequent precipitation, its signal can be inherited in the resulting precipitation (Risi et al., 2008b). However, a clear relationship between TP precipitation d -excess and monsoon convection has yet to be established, partly due to limited attention paid to d -excess in previous studies (Yao et al., 2013). On the other hand, local raindrop evaporation may counteract this effect by reducing raindrop d -excess values. The overall positive correlation between precipitation d -excess and altitude across Asia has sometimes been attributed to stronger evaporation at lower altitudes (Bershaw, 2018). For snowfall on glaciers, however, evaporation for falling snowflakes is less likely due to cold temperatures and the short distance between the cloud base and the glacier surface. Therefore, elevated vapor d -excess signals caused by accumulated rain-vapor interactions at upstream associated with monsoon convection could be another possible source of the high d -excess in ice cores.

5 Conclusions

We present a three-year daily near-surface vapor isotope dataset collected at the SETP station, which is at the

major channel for moisture entering the TP. The paired measurements of vapor isotopes and specific humidity reveal distinct moisture sources and dynamics between non-monsoon and summer monsoon seasons, consistent with findings from Lagrangian moisture diagnostic. Despite significant negative correlations between d -excess and normalized RH over the northern Indian Ocean when all seasons are considered, these correlations weaken or even disappear when analyzed within individual seasons.

During the non-monsoon season, vapor d -excess is primarily influenced by specific humidity at both local and upstream scales. Air that has undergone significant dehydration, situated at the lower end of the Rayleigh distillation, is expected to have extremely high d -excess values. Backward trajectory analyses and moisture source diagnostics reveal that the intrusion of cold and dry air driven by westerlies during the non-monsoon season leads to the increasing trend in d -excess as specific humidity decreases. This process also contributes to a weak negative correlation between d -excess and $\delta^{18}\text{O}$. Furthermore, $\delta^{18}\text{O}$ primarily reflects mixing processes involving a relatively enriched moist end-member compared to the summer monsoon season.

During the summer monsoon season, rain evaporation and “super-Rayleigh” processes emerge as the dominant process shaping vapor isotope compositions. First, $\delta^{18}\text{O}$ systematically shifts below the Rayleigh distillation curve, aligning with predictions of “super-Rayleigh” distillation caused by partial rain evaporation. Second, $\delta^{18}\text{O}$ is anti-correlated with d -excess, pointing to kinetic fractionation as a source of depleted vapor, which cannot be attributed solely to rainout. Third, at the regional scale, $\delta^{18}\text{O}$ shows significant negative correlations with total precipitation amount, while d -excess positively correlates with total precipitation amount.

These findings will aid in interpreting $\delta^{18}\text{O}$ and d -excess records from Tibetan Plateau glaciers, offering refined insights into past hydroclimatic conditions and challenging assumptions linking ice core isotopes to oceanic evaporation alone. The new insights into vapor d -excess during the non-monsoon season provide an alternative framework for interpreting the high d -excess in high-altitude TP ice cores. The introduction of high d -excess values

532 by subsidence air from high altitudes could likely be a general phenomenon, as similar findings have been reported
533 elsewhere (Samuels - Crow et al., 2014; Sodemann et al., 2017). Additionally, the findings on summer monsoon
534 season moisture dynamics help disentangle the different effects of rainout and rain-vapor interactions in the context
535 of the amount effect (Bowen et al., 2019; Galewsky et al., 2016). While this study questions the earlier interpretation
536 of TP *d*-excess as an indicator of oceanic evaporation conditions (Zhao et al., 2012; Shao et al., 2021; Chen et al.,
537 2024; Liu et al., 2024), other studies have also raised doubts about the preservation of these signals inland (Fiorella
538 et al., 2018; Aemisegger et al., 2014; Welp et al., 2012; Wei and Lee, 2019; Samuels - Crow et al., 2014). Further
539 research is needed to determine how far inland oceanic evaporation signals can be preserved during the transport
540 from coastal areas. Moreover, we acknowledge the use of simplistic assumptions regarding the isotopic
541 compositions of evapotranspiration fluxes, highlighting the need for deeper investigation into the isotopic
542 compositions of these fluxes to comprehend the effect of continental recycling. Furthermore, the focus on lower
543 tropospheric vapor sources contrasts with precipitation sources at higher levels, which may differ and require
544 additional exploration. Finally, the resolution of meteorological data may influence the accuracy of trajectory
545 calculation and moisture tracking results. Future research should consider utilizing higher-resolution meteorological
546 data or implementing regional high-resolution models to enhance the precision of these analyses.

547 **Competing interests**

548 The authors declare that they have no conflict of interest.

549 **Acknowledgements**

550 We thank the editors and the referees for their comments and suggestions. This research was supported by the
551 National Key R&D Program of China (Grant 2024YFF0807901), the National Natural Science Foundation of China
552 (Grant 42371144), the Yunnan Fundamental Research Projects (Grant 202301AT070183), and the funding of

553 Donglu Talent Young Scholar from the Yunnan University and support for young scholars from the Double First-
554 Class Initiative for Ecological Disciplines of the Yunnan University. We would like to thank the staff at the South-
555 East Tibetan Plateau Station for integrated observation and research of alpine environment for their help in collecting
556 water samples and for sharing the meteorological data at the station.

557 **Data availability**

558 The NOAA ARL provided the HYSPLIT model and the GDAS data
559 (<https://www.ready.noaa.gov/HYSPLIT.php>). The Copernicus Climate Change Service provided the ERA5 data
560 (<https://doi.org/10.24381/cds.adbb2d47> and <https://doi.org/10.24381/cds.fl7050d7>). The GPM data are available
561 through GES DISC (<https://doi.org/10.5067/GPM/IMERG/3B-HH/07>). Local meteorological data at the SETP
562 station are provided by National Tibetan Plateau / Third Pole Environment Data Center
563 (<https://dx.doi.org/10.11888/AtmosphericPhysics.tpe.68.db>). The observation data at the SETP station have been
564 uploaded to Figshare and will be made publicly available after publication (10.6084/m9.figshare.27302871).

565 **Author contributions**

566 **Zhongyin Cai**: Conceptualization, methodology, investigation, formal analysis, funding acquisition, writing-
567 original draft, writing-review & editing; **Rong Li**: Investigation, data curation, writing-review & editing; **Cheng**
568 **Wang**: Validation; **Qiukai Mao**: Investigation, **Lide Tian**: Resources, project administration, funding acquisition.

569 **References**

570

571 Aemisegger, F., Pfahl, S., Sodemann, H., Lehner, I., Seneviratne, S. I., and Wernli, H.: Deuterium excess as a
572 proxy for continental moisture recycling and plant transpiration, *Atmos. Chem. Phys.*, 14, 4029–4054, 10.5194/acp-
573 14-4029-2014, 2014.
574 An, W., Hou, S., Zhang, Q., Zhang, W., Wu, S., Xu, H., Pang, H., Wang, Y., and Liu, Y.: Enhanced Recent Local

575 Moisture Recycling on the Northwestern Tibetan Plateau Deduced From Ice Core Deuterium Excess Records, *J.*
576 *Geophys. Res.*, 122, 511-522, 10.1002/2017jd027235, 2017.

577 Araguás-Araguás, L., Fröhlich, K., and Rozanski, K.: Stable isotope composition of precipitation over
578 southeast Asia, *J. Geophys. Res.*, 103, 28721-28742, 1998.

579 Benetti, M., Reverdin, G., Pierre, C., Merlivat, L., Risi, C., Steen-Larsen, H. C., and Vimeux, F.: Deuterium excess
580 in marine water vapor: Dependency on relative humidity and surface wind speed during evaporation, *J. Geophys.*
581 *Res.*, 119, 584-593, 2014.

582 Bershaw, J.: Controls on Deuterium Excess across Asia, *Geosciences*, 8, 257, 10.3390/geosciences8070257,
583 2018.

584 Bonne, J.-L., Behrens, M., Meyer, H., Kipfstuhl, S., Rabe, B., Schönicke, L., Steen-Larsen, H. C., and Werner, M.:
585 Resolving the controls of water vapour isotopes in the Atlantic sector, *Nature Communications*, 10, 1632,
586 10.1038/s41467-019-09242-6, 2019.

587 Bonne, J. L., Masson-Delmotte, V., Cattani, O., Delmotte, M., Risi, C., Sodemann, H., and Steen-Larsen, H. C.:
588 The isotopic composition of water vapour and precipitation in Ivittuut, southern Greenland, *Atmos. Chem. Phys.*,
589 14, 4419-4439, 10.5194/acp-14-4419-2014, 2014.

590 Bony, S., Risi, C., and Vimeux, F.: Influence of convective processes on the isotopic composition ($\delta^{18}\text{O}$ and δD)
591 of precipitation and water vapor in the tropics: 1. Radiative-convective equilibrium and Tropical Ocean–Global
592 Atmosphere–Coupled Ocean–Atmosphere Response Experiment (TOGA-COARE) simulations, *J. Geophys. Res.*,
593 113, D19305, 10.1029/2008JD009942, 2008.

594 Bowen, G. J. and Wilkinson, B.: Spatial distribution of $\delta^{18}\text{O}$ in meteoric precipitation, *Geology*, 30, 315,
595 10.1130/0091-7613(2002)030<0315:sdooim>2.0.co;2, 2002.

596 Bowen, G. J., Cai, Z., Fiorella, R. P., and Putman, A.: Isotopes in the Water Cycle: Regional- to Global-Scale
597 Patterns and Applications, *Annu. Rev. Earth Planet. Sci.*, 47, 453-479, 10.1146/annurev-earth-053018-060220,
598 2019.

599 Breitenbach, S. F. M., Adkins, J. F., Meyer, H., Marwan, N., Kumar, K. K., and Haug, G. H.: Strong influence of
600 water vapor source dynamics on stable isotopes in precipitation observed in Southern Meghalaya, NE India, *Earth*
601 *Planet. Sci. Lett.*, 292, 212-220, 10.1016/j.epsl.2010.01.038, 2010.

602 Cai, Z. and Tian, L.: Atmospheric controls on seasonal and interannual variations in the precipitation isotope
603 in the East Asian Monsoon region, *J. Climate*, 29, 1339-1352, 10.1175/JCLI-D-15-0363.1, 2016.

604 Cai, Z. and Tian, L.: What causes the post-monsoon ^{18}O depletion over Bay of Bengal head and beyond?,
605 *Geophys. Res. Lett.*, 47, e2020GL086985, 10.1029/2020gl086985, 2020.

606 Cai, Z., Tian, L., and Bowen, G. J.: ENSO variability reflected in precipitation oxygen isotopes across the Asian
607 Summer Monsoon region, *Earth Planet. Sci. Lett.*, 475, 25-33, 10.1016/j.epsl.2017.06.035, 2017.

608 Cai, Z., Tian, L., and Bowen, G. J.: Spatial-seasonal patterns reveal large-scale atmospheric controls on Asian
609 Monsoon precipitation water isotope ratios, *Earth Planet. Sci. Lett.*, 503, 158-169, 10.1016/j.epsl.2018.09.028, 2018.

610 Cai, Z., Li, R., Wang, C., and Tian, L.: Atmospheric controls on precipitation isotopes in North China and their
611 response to record-breaking torrential rainfall, *J. Hydrol.*, 661, 10.1016/j.jhydrol.2025.133762, 2025.

612 Cao, R., Huang, H., Wu, G., Han, D., Jiang, Z., Di, K., and Hu, Z.: Spatiotemporal variations in the ratio of
613 transpiration to evapotranspiration and its controlling factors across terrestrial biomes, *Agr. Forest Meteorol.*, 321,
614 108984, 10.1016/j.agrformet.2022.108984, 2022.

615 Chen, M., Gao, J., Luo, L., Zhao, A., Niu, X., Yu, W., Liu, Y., and Chen, G.: Temporal variations of stable isotopic
616 compositions in atmospheric water vapor on the Southeastern Tibetan Plateau and their controlling factors, *Atmos.*
617 *Res.*, 303, 10.1016/j.atmosres.2024.107328, 2024.

618 Craig, H.: Isotopic Variations in Meteoric Waters, *Science*, 133, 1702-1703, 10.1126/science.133.3465.1702,

1961.

Craig, H. and Gordon, L. I.: Deuterium and oxygen 18 variations in the ocean and the marine atmosphere, in: Stable Isotopes in Oceanographic Studies and Paleotemperatures. Spoleto, Tongiorgi, E., Italy, 9-130, 1965.

Dai, D., Gao, J., Steen-Larsen, H. C., Yao, T., Ma, Y., Zhu, M., and Li, S.: Continuous monitoring of the isotopic composition of surface water vapor at Lhasa, southern Tibetan Plateau, Atmos. Res., 264, 10.1016/j.atmosres.2021.105827, 2021.

Dansgaard, W.: Stable isotopes in precipitation, Tellus, 16, 436-468, 10.1111/j.2153-3490.1964.tb00181.x, 1964.

Dütsch, M., Pfahl, S., and Sodemann, H.: The impact of nonequilibrium and equilibrium fractionation on two different deuterium excess definitions, J. Geophys. Res., 122, 12732-12746, 10.1002/2017JD027085, 2017.

Fiorella, R. P., Poulsen, C. J., and Matheny, A. M.: Seasonal Patterns of Water Cycling in a Deep, Continental Mountain Valley Inferred from Stable Water Vapor Isotopes, J. Geophys. Res., 123, 7271-7291, doi:10.1029/2017JD028093, 2018.

Galewsky, J., Steen-Larsen, H. C., Field, R. D., Worden, J., Risi, C., and Schneider, M.: Stable isotopes in atmospheric water vapor and applications to the hydrologic cycle, Rev. Geophys., 54, 809-865, 10.1002/2015RG000512, 2016.

Good, S. P., Noone, D., and Bowen, G.: Hydrologic connectivity constrains partitioning of global terrestrial water fluxes, Science, 349, 175-177, 10.1126/science.aaa5931, 2015.

Guo, H., Pang, H., Wu, S., Xu, T., Mutz, S. G., Zhan, Z., Lin, W., Zhang, W., and Hou, S.: Global abnormal precipitation ^{18}O depletion during late/post monsoon season, Earth Planet. Sci. Lett., 641, 10.1016/j.epsl.2024.118815, 2024.

Han, J., Tian, L., Cai, Z., Ren, W., Liu, W., Li, J., and Tai, J.: Season-specific evapotranspiration partitioning using dual water isotopes in a Pinus yunnanensis ecosystem, southwest China, J. Hydrol., 608, 127672, 10.1016/j.jhydrol.2022.127672, 2022.

He, S., Jackisch, D., Feng, L., Samanta, D., Wang, X., and Goodkin, N. F.: Uncovering Below Cloud Rain-Vapor Interactions During Tropical Rain Events Through Simultaneous and Continuous Real-Time Monitoring of Rain and Vapor Isotopes, J. Geophys. Res., 129, e2023JD040084, <https://doi.org/10.1029/2023JD040084>, 2024.

He, Y., Risi, C., Gao, J., Masson-Delmotte, V., Yao, T., Lai, C.-T., Ding, Y., Worden, J., Frankenberg, C., Chepfer, H., and Cesana, G.: Impact of atmospheric convection on south Tibet summer precipitation isotopologue composition using a combination of in situ measurements, satellite data and atmospheric general circulation modeling, J. Geophys. Res., 120, 3852-3871, 10.1002/2014JD022180, 2015.

Hersbach, H., Bell, B., Berrisford, P., Horányi, A., J., M.-S., Nicolas, J., Radu, R., Schepers, D., Simmons, A., Soci, C., and Dee, D.: Global reanalysis: goodbye ERA-Interim, hello ERA5, 10.21957/vf291hehd7, 2019.

Huang, J.: A Simple Accurate Formula for Calculating Saturation Vapor Pressure of Water and Ice, Journal of Applied Meteorology and Climatology, 57, 1265-1272, JAMC-D-17-0334.1, 2018.

Huffman, G. J., Stocker, E. F., Bolvin, D. T., Nelkin, E. J., and Tan, J.: GPM IMERG Final Precipitation L3 Half Hourly 0.1 degree x 0.1 degree V07, Greenbelt, MD, Goddard Earth Sciences Data and Information Services Center (GES DISC) [dataset], 10.5067/GPM/IMERG/3B-HH/07, 2023.

Immerzeel, W. W., Lutz, A. F., Andrade, M., Bahl, A., Biemans, H., Bolch, T., Hyde, S., Brumby, S., Davies, B. J., Elmore, A. C., Emmer, A., Feng, M., Fernández, A., Haritashya, U., Kargel, J. S., Koppes, M., Kraaijenbrink, P. D. A., Kulkarni, A. V., Mayewski, P. A., Nepal, S., Pacheco, P., Painter, T. H., Pellicciotti, F., Rajaram, H., Rupper, S., Sinisalo, A., Shrestha, A. B., Viviroli, D., Wada, Y., Xiao, C., Yao, T., and Baillie, J. E. M.: Importance and vulnerability of the world's water towers, Nature, 577, 364-369, 10.1038/s41586-019-1822-y, 2020.

Jiang, J., Zhou, T., Qian, Y., Li, C., Song, F., Li, H., Chen, X., Zhang, W., and Chen, Z.: Precipitation regime

changes in High Mountain Asia driven by cleaner air, *Nature*, 10.1038/s41586-023-06619-y, 2023.

Joswiak, D. R., Yao, T., Wu, G., Tian, L., and Xu, B.: Ice-core evidence of westerly and monsoon moisture contributions in the central Tibetan Plateau, *J. Glaciol.*, 59, 56-66, 10.3189/2013JoG12J035, 2013.

Keeling, C. D.: The concentration and isotopic abundances of atmospheric carbon dioxide in rural areas, *Geochim. Cosmochim. Acta*, 13, 322-334, 10.1016/0016-7037(58)90033-4, 1958.

Kurita, N., Fujiyoshi, Y., Nakayama, T., Matsumi, Y., and Kitagawa, H.: East Asian Monsoon controls on the inter-annual variability in precipitation isotope ratio in Japan, *Climate of the Past*, 11, 339-353, 10.5194/cp-11-339-2015, 2015.

Kurita, N., Noone, D., Risi, C., Schmidt, G. A., Yamada, H., and Yoneyama, K.: Intraseasonal isotopic variation associated with the Madden-Julian Oscillation, *J. Geophys. Res.*, 116, D24101, 10.1029/2010JD015209, 2011.

Lawrence, J. R., Gedzelman, S. D., Dexheimer, D., Cho, H.-K., Carrie, G. D., Gasparini, R., Anderson, C. R., Bowman, K. P., and Biggerstaff, M. I.: Stable isotopic composition of water vapor in the tropics, *J. Geophys. Res.*, 109, D06115, 10.1029/2003JD004046, 2004.

Lee, J.-E. and Fung, I.: "Amount effect" of water isotopes and quantitative analysis of post-condensation processes, *Hydrol. Processes*, 22, 1-8, 10.1002/hyp.6637, 2008.

Li, R., Cai, Z., Wang, C., Liu, F., Yang, D., Xu, C., Yu, S., Yu, X., Fan, Q., and Tian, L.: Multiple Climate Forcings Decomposed From a Tibetan Plateau Ice Core Isotope Record, *J. Geophys. Res.*, 130, e2024JD042929, <https://doi.org/10.1029/2024JD042929>, 2025.

Liu, F., Tian, L., Cai, Z., Wang, X., Liang, P., Wang, S., and Li, S.: What caused the lag between oxygen-18 and deuterium excess in atmospheric vapor and precipitation during the earlier summer season in southwest China?, *J. Hydrol.*, 644, 10.1016/j.jhydrol.2024.132087, 2024.

Liu, J., Xiao, C., Ding, M., and Ren, J.: Variations in stable hydrogen and oxygen isotopes in atmospheric water vapor in the marine boundary layer across a wide latitude range, *Journal of Environmental Sciences*, 26, 2266-2276, 10.1016/j.jes.2014.09.007, 2014.

Luo, L.: Meteorological observation data from the integrated observation and research station of the alpine environment in Southeast Tibet (2007-2017), National Tibetan Plateau Data Center [dataset], 10.11888/AtmosphericPhysics.tpe.68.db, 2018.

Ma, T., Jiang, Z., Ding, M., He, P., Li, Y., Zhang, W., and Geng, L.: A model framework for atmosphere-snow water vapor exchange and the associated isotope effects at Dome Argus, Antarctica – Part 1: The diurnal changes, *The Cryosphere*, 18, 4547-4565, 10.5194/tc-18-4547-2024, 2024.

Merlivat, L. and Jouzel, J.: Global climatic interpretation of the deuterium - oxygen 18 relationship for precipitation, *J. Geophys. Res.*, 84, 5029-5033, 1979.

Noone, D.: Pairing Measurements of the Water Vapor Isotope Ratio with Humidity to Deduce Atmospheric Moistening and Dehydration in the Tropical Midtroposphere, *J. Climate*, 25, 4476-4494, 10.1175/jcli-d-11-00582.1, 2012.

Pang, H., Hou, S., Kaspari, S., Mayewski, P., Introne, D., Masson-Delmotte, V., Jouzel, J., Li, Z., He, Y., Hong, S., and Qin, D.: Atmospheric circulation change in the central Himalayas indicated by a high-resolution ice core deuterium excess record, *Climate Research*, 53, 1-12, 10.3354/cr01090, 2012.

Putman, A. L., Fiorella, R. P., Bowen, G. J., and Cai, Z.: A Global Perspective on Local Meteoric Water Lines: Meta-analytic Insight into Fundamental Controls and Practical Constraints, *Water Resour. Res.*, 55, 6896-6910, 10.1029/2019wr025181, 2019.

Risi, C., Bony, S., and Vimeux, F.: Influence of convective processes on the isotopic composition ($\delta^{18}\text{O}$ and δD) of precipitation and water vapor in the tropics: 2. Physical interpretation of the amount effect, *J. Geophys. Res.*, 113, D19306, 10.1029/2008JD009943, 2008a.

707 Risi, C., Bony, S., Vimeux, F., Descroix, L., Ibrahim, B., Lebreton, E., Mamadou, I., and Sultan, B.: What controls
708 the isotopic composition of the African monsoon precipitation? Insights from event-based precipitation collected
709 during the 2006 AMMA field campaign, *Geophys. Res. Lett.*, 35, L24808, 10.1029/2008GL035920, 2008b.

710 Ruan, J., Zhang, H., Cai, Z., Yang, X., and Yin, J.: Regional controls on daily to interannual variations of
711 precipitation isotope ratios in Southeast China: Implications for paleomonsoon reconstruction, *Earth Planet. Sci.*
712 *Lett.*, 527, 115794, 10.1016/j.epsl.2019.115794, 2019.

713 Samuels-Crow, K. E., Galewsky, J., Sharp, Z. D., and Dennis, K. J.: Deuterium excess in subtropical free
714 troposphere water vapor: Continuous measurements from the Chajnantor Plateau, northern Chile, *Geophys. Res.*
715 *Lett.*, 41, 8652-8659, 10.1002/2014gl062302, 2014.

716 Shao, L., Tian, L., Cai, Z., Wang, C., and Li, Y.: Large-scale atmospheric circulation influences the ice core d-
717 excess record from the central Tibetan Plateau, *Clim. Dyn.*, 57, 1805-1816, 10.1007/s00382-021-05779-9, 2021.

718 Sodemann, H., Schwierz, C., and Wernli, H.: Interannual variability of Greenland winter precipitation sources:
719 Lagrangian moisture diagnostic and North Atlantic Oscillation influence, *J. Geophys. Res.*, 113,
720 10.1029/2007jd008503, 2008.

721 Sodemann, H., Aemisegger, F., Pfahl, S., Bitter, M., Corsmeier, U., Feuerle, T., Graf, P., Hankers, R., Hsiao, G.,
722 Schulz, H., Wieser, A., and Wernli, H.: The stable isotopic composition of water vapour above Corsica during the
723 HyMeX SOP1 campaign: insight into vertical mixing processes from lower-tropospheric survey flights, *Atmos.*
724 *Chem. Phys.*, 17, 6125-6151, 10.5194/acp-17-6125-2017, 2017.

725 Steen-Larsen, H. C., Risi, C., Werner, M., Yoshimura, K., and Masson-Delmotte, V.: Evaluating the skills of
726 isotope-enabled General Circulation Models against in-situ atmospheric water vapor isotope observations, *J.*
727 *Geophys. Res.*, 122, 246-263, 10.1002/2016JD025443, 2017.

728 Stein, A. F., Draxler, R. R., Rolph, G. D., Stunder, B. J. B., Cohen, M. D., and Ngan, F.: NOAA's HYSPLIT
729 atmospheric transport and dispersion modeling system, *Bull. Am. Meteorol. Soc.*, 96, 2059-2077, 10.1175/BAMS-
730 D-14-00110.1, 2015.

731 Terzer-Wassmuth, S., Wassenaar, L. I., Welker, J. M., and Araguas-Araguas, L. J.: Improved High-Resolution
732 Global and Regionalized Isoscapes of $\delta^{18}\text{O}$, $\delta^2\text{H}$, and d-Excess in Precipitation, *Hydrol. Processes*, 35,
733 10.1002/hyp.14254, 2021.

734 Thompson, L. G., Yao, T., E.Mosley-Thompson, Davis, M. E., Henderson, K. A., and Lin, P.-N.: A High-
735 Resolution Millennial Record of the South Asian Monsoon from Himalayan Ice Cores, *Science*, 289, 1916-1919,
736 10.1126/science.289.5486.1916, 2000.

737 Thompson, L. G., Yao, T. D., Davis, M. E., Mosley-Thompson, E., Synal, H. A., Wu, G., Bolzan, J. F., Kutuzov, S.,
738 Beaudon, E., Sierra-Hernández, M. R., and Beer, J.: Ice core evidence for an orbital-scale climate transition on the
739 Northwest Tibetan Plateau, *Quat. Sci. Rev.*, 324, 10.1016/j.quascirev.2023.108443, 2024.

740 Tian, L., Masson-Delmotte, V., Stievenard, M., Yao, T., and Jouzel, J.: Tibetan Plateau summer monsoon
741 northward extent revealed by measurements of water stable isotopes, *J. Geophys. Res.*, 106, 28081-28088,
742 10.1029/2001JD900186, 2001.

743 Tian, L., Yao, T., MacClune, K., White, J. W. C., Schilla, A., Vaughn, B., Vachon, R., and Ichiyanagi, K.: Stable
744 isotopic variations in west China: A consideration of moisture sources, *J. Geophys. Res.*, 112, D10112,
745 10.1029/2006jd007718, 2007.

746 Tian, L., Yu, W., Schuster, P. F., Wen, R., Cai, Z., Wang, D., Shao, L., Cui, J., and Guo, X.: Control of seasonal
747 water vapor isotope variations at Lhasa, southern Tibetan Plateau, *J. Hydrol.*, 580, 124237,
748 10.1016/j.jhydrol.2019.124237, 2020.

749 Uemura, R., Matsui, Y., Yoshimura, K., Motoyama, H., and Yoshida, N.: Evidence of deuterium excess in water
750 vapor as an indicator of ocean surface conditions, *J. Geophys. Res.*, 113, 10.1029/2008jd010209, 2008.

Wahl, S., Steen-Larsen, H. C., Hughes, A. G., Dietrich, L. J., Zuhr, A., Behrens, M., Faber, A.-K., and Hörhold, M.: Atmosphere-Snow Exchange Explains Surface Snow Isotope Variability, *Geophys. Res. Lett.*, 49, e2022GL099529, 10.1029/2022GL099529, 2022.

Webster, C. R. and Heymsfield, A. J.: Water isotope ratios D/H, 18O/16O, 17O/16O in and out of clouds map dehydration pathways, *Science*, 302, 1742–1745, 10.1126/science.1089496, 2003.

Wei, Z. and Lee, X.: The utility of near-surface water vapor deuterium excess as an indicator of atmospheric moisture source, *J. Hydrol.*, 123923, 10.1016/j.jhydrol.2019.123923, 2019.

Welp, L. R., Lee, X., Griffis, T. J., Wen, X. F., Xiao, W., Li, S., Sun, X., Hu, Z., Val Martin, M., and Huang, J.: A meta-analysis of water vapor deuterium-excess in the midlatitude atmospheric surface layer, *Global Biogeochem. Cycles*, 26, 10.1029/2011gb004246, 2012.

Worden, J., Noone, D., and Bowman, K.: Importance of rain evaporation and continental convection in the tropical water cycle, *Nature*, 445, 528–532, 10.1038/nature05508, 2007.

Yang, X. and Yao, T.: Seasonality of moisture supplies to precipitation over the Third Pole: a stable water isotopic perspective, *Sci Rep*, 10, 15020, 10.1038/s41598-020-71949-0, 2020.

Yang, X., Davis, M. E., Acharya, S., and Yao, T.: Asian monsoon variations revealed from stable isotopes in precipitation, *Clim. Dyn.*, 51, 2267–2283, 10.1007/s00382-017-4011-4, 2017.

Yao, T., Masson-Delmotte, V., Gao, J., Yu, W., Yang, X., Risi, C., Sturm, C., Werner, M., Zhao, H., He, Y., Ren, W., Tian, L., Shi, C., and Hou, S.: A review of climatic controls on $\delta^{18}\text{O}$ in precipitation over the Tibetan Plateau: Observations and simulations, *Rev. Geophys.*, 51, 525–548, 10.1002/rog.20023, 2013.

Yao, T., Bolch, T., Chen, D., Gao, J., Immerzeel, W., Piao, S., Su, F., Thompson, L., Wada, Y., Wang, L., Wang, T., Wu, G., Xu, B., Yang, W., Zhang, G., and Zhao, P.: The imbalance of the Asian water tower, *Nature Reviews Earth & Environment*, 3, 618–632, 10.1038/s43017-022-00299-4, 2022.

Yu, W., Tian, L., Ma, Y., Xu, B., and Qu, D.: Simultaneous monitoring of stable oxygen isotope composition in water vapour and precipitation over the central Tibetan Plateau, *Atmos. Chem. Phys.*, 15, 10251–10262, 10.5194/acp-15-10251-2015, 2015.

Yu, W., Tian, L., Risi, C., Yao, T., Ma, Y., Zhao, H., Zhu, H., He, Y., Xu, B., Zhang, H., and Qu, D.: $\delta^{18}\text{O}$ records in water vapor and an ice core from the eastern Pamir Plateau: Implications for paleoclimate reconstructions, *Earth Planet. Sci. Lett.*, 456, 146–156, 10.1016/j.epsl.2016.10.001, 2016.

Zhang, Q., Shen, Z., Pokhrel, Y., Farinotti, D., Singh, V. P., Xu, C.-Y., Wu, W., and Wang, G.: Oceanic climate changes threaten the sustainability of Asia's water tower, *Nature*, 615, 87–93, 10.1038/s41586-022-05643-8, 2023.

Zhang, Q., Shen, Z., Pokhrel, Y., Farinotti, D., Singh, V. P., Xu, C.-Y., Wu, W., and Wang, G.: Reply to: Atlantic oceanic droughts do not threaten Asian water tower, *Nature*, 638, E16–E18, 10.1038/s41586-024-08358-0, 2025.

Zhao, H., Xu, B., Li, Z., Wang, M., Li, J., and Zhang, X.: Abundant climatic information in water stable isotope record from a maritime glacier on southeastern Tibetan Plateau, *Clim. Dyn.*, 48, 1161–1171, 10.1007/s00382-016-3133-4, 2017.

Zhao, H., Xu, B., Yao, T., Wu, G., Lin, S., Gao, J., and Wang, M.: Deuterium excess record in a southern Tibetan ice core and its potential climatic implications, *Clim. Dyn.*, 38, 1791–1803, 10.1007/s00382-011-1161-7, 2012.

Zhao, Y., Xu, C., Yu, X., Liu, Y., and Ji, X.: Atlantic oceanic droughts do not threaten Asian water tower, *Nature*, 638, E13–E15, 10.1038/s41586-024-08357-1, 2025.